A study of secondary pyrite deformation and calcite veins in SAFOD damage zone with implications for aseismic creep deformation mechanism at depths >3km

Jafar Hadizadeh[1] and Alan P. Boyle[2]

[1] Department of Geography & Geosciences, University of Louisville, Louisville KY 40292, USA
[2] Department of Earth Ocean & Ecological Sciences, University of Liverpool, Liverpool, U.K.

Abstract

Previous studies of the San Andreas Fault damage-zone samples from the San Andreas Fault Observatory at Depth (SAFOD) have identified a variety of tectonic microstructures including pressure solution cleavage, calcite-sealed fractures vein fabric, and pyrite and anhydrite hydrothermal fracture sealing. Understanding the deformation provenance of the damage zone rocks and operative deformation mechanism(s) based on preserved microstructures provide insight into overall deformation behavior of the entire seismogenic zone in the creeping section of this transform fault. We analyzed the deformation of hydrothermal secondary pyrite in connection with network of calcite veins in a sample of foliated ultracataclasites bordering the actively creeping Southwestern Deforming Zone (SDZ), using SEM, EBSD and CL microscopy. The results show that calcite veins associated with the pressure solution cleavage are crosscut by the secondary pyrite deformed under a range of P-T conditions. Relatively undeformed secondary pyrite is found sealing implosion microbreccia. Our review of previously available data indicates that the damage zone rocks may represent a collage of structural and compositional domains from both locked and creeping sections of the SAF. This interpretation together with results of this study suggest that weak-clay frictional deformation mechanism(s) is likely to be the predominant aseismic creep mechanism at depths below the SAFOD.

Keywords: SAFOD; Deformation of pyrite; Calcite-vein Cathodoluminescence; Aseismic creep in the SAF; Pressure solution.

1. Introduction

Plate-scale faults are active for extended periods of Earth history. They involve ductile deformation mechanisms at depth and brittle mechanisms nearer the surface, and act as conduits for typically bisulphide ion (HS^{-})-bearing low-salinity H_2O-CO_2 fluids escaping from metamorphic and/or igneous activity at depth (Goldfarb and Groves 2015). These fluids are often inferred to initiate deformation on faults via episodic over-pressuring leading to fault-valve or seismic pumping mechanisms (Cox, 1995; Sibson, 1981, 1990, 1992, and 1994). Episodic pumping of the fluids leads to decompression-related breakdown of the H_2O-CO_2 fluid as well as the HS^- ligand complexes leading to carbonate precipitation associated with pyrite (McCuaig and Kerrich, 1998). This behavior gives rise to the interesting possibility that episodic formation of calcite and pyrite in an actively deforming fault could preserve significant parts of fault histories. Recently, Holdsworth et al. (2011) and Bradbury et al. (2015) described the ubiquitous development of calcite-filled veins and disseminated pyrite suggesting that the San Andreas Fault Observatory at Depth (SAFOD) may be a suitable place to investigate the potential for calcite and pyrite microstructures to record the fault deformation history.

Understanding of pyrite deformation mechanisms and microstructures over a wide range of temperature conditions has expanded significantly over the last 20 years through using electron backscatter diffraction (EBSD) methods (Barrie et al., 2007, 2008, 2010a; Boyle et al., 1998; Reddy and Hough, 2013). Pyrite is a robust, refractory mineral well suited to preserving evidence of any plastic or brittle deformation it has experienced below ~650°C and thus has potential for preserving a memory of deformation over a range of temperature conditions. For most of the 20th century, pyrite was thought to undergo a brittle-crystal plastic transition above ~400°C, though grain growth and annealing were considered more likely above that temperature (McClay and Ellis, 1983). Extensive EBSD-driven research has recently demonstrated that pyrite behaves in a crystal-plastic manner to much lower temperatures of ~250°C (Barrie et al., 2009; Freitag et al., 2004). The EBSD-based research has also developed a new deformation-mechanism map for pyrite reflecting the much wider range of conditions for which it will deform by dislocation creep or glide (Barrie et al., 2011).

This paper seeks to explore the hypothesis that segments of fault history can be determined through study of episodically developed calcite and pyrite microstructures, which are two minerals that are commonly developed in faults. More specifically, the study is focused on understanding the microstructural and mechanical implications of deformation of the pyrite in association with calcite veins for possible creep deformation mechanisms below the SAFOD depths. It has been argued that deformation by pressure solution is a viable creep mechanism throughout the entire seismogenic zone (Gratier et al., 2011; Richard et al., 2014). On the other hand, several studies have suggested that the weak-clay frictional deformation mechanisms similar to those observed in SDZ and CDZ are likely to operate at depths below the SAFOD and probably over the entire seismogenic profile (e.g. Carpenter et al., 2012; French et al., 2015; Carpenter et al., 2015; Moore et al., 2016). The latter model is supported by experimental work (Moore and Lockner, 2011; Moore and Lockner, 2013) and studies of fault-rock outcrops in the creeping segment of the SAF that suggest the creep behavior involves a continuous generation of low-friction smectite clays due to entrainment of serpentinite bodies in this section of the fault over the past 2.5 million years (Page et al. 1998; Titus et al. 2011). Experimental work by Bos and Spires (2001and 2002) indicates that a hybrid deformation mechanism model involving frictional-viscous flow of phyllosilicates and pressure solution may be applicable to mature fault zones. A firm understanding of the mechanism of aseismic creep and its evolution over the entire seismogenic profile would provide insight into the question about the potential for damaging seismic ruptures in the creeping section of the SAF.

2. The SAFOD sample

The SAFOD is sited on the Pacific plate 1.8 km southwest of the surface trace of the San Andreas Fault, and 9 km northwest of Parkfield, California. The observatory's ~4km long drill hole (~2.77km vertical) penetrates Salinian block in the Pacific plate and turns northeast across the fault into the Great Valley/Franciscan block in the North American plate. The geologic setting of the site indicates contractional, extensional and strike-slip deformation with the resulting structural and material complexities. The plate motion in the central section of the SAF, including at the SAFOD site, is accommodated via aseismic creep. For detailed lithological descriptions and further information regarding the geology and seismotectonics in the vicinity of the SAFOD, the reader is referred to other studies (e.g. McPhee et al. 2004, Thayer et al., 2004, Arrowsmith et al. 2005, Titus et al. 2006, Bradbury et al. 2007and 2011, and Holdsworth et al. 2012).

This study is based on two polished thin sections from a single sample with well-developed calcite-filled veins in clasts and matrix of the cataclasites and the presence of significant pyrite. The use of a single suitable sample is vindicated by the main aim of this paper which is to investigate the hypothesis that segments of fault history can be determined through study of episodically developed calcite and pyrite microstructures. We want to see if combined study of calcite and pyrite microstructures can provide a tool to document otherwise unavailable information about fault evolution through time. While other studies of SAFOD have studied multiple samples (e.g. Moore and Rymer, 2007: Carpenter et al., 2009 and 2011; Bradbury et al., 2011; Schleicher et al., 2009a, 2009b, 2010, and 2012; Janssen et al., 2012; Lockner et al., 2011; Moore and Rymer, 2012; Hadizadeh et al., 2012; Moore and Lockner, 2013; Moore, 2014; Warr et al., 2014; Morrow et al., 2014), none have addressed the potential combined use of calcite and pyrite to elucidate fault history. Successful demonstration of using calcite and pyrite as tools for determining SAFOD history should encourage their use in a wider range of samples.

Our sample was extracted as a billet measuring ~75×70×50 mm from interval 3193.91m to 3193.98m Measured Depth (MD) of run 2, core section 4 of the lateral borehole G (Fig. 1a). The core sample through the fault rock consists of a hard, dark-colored foliated siltstone-shale ultracataclasite with visible veins running sub-parallel to foliation (Fig. 1b). Note that although the ultracataclasite is a cohesive fault rock, we simply refer to it as the gouge. The sample billet included a sharp border with a massive gray-black shale toward the core bottom (NE end of the core section).

The lateral boreholes depicted in Fig. 1a were drilled in phase III of the SAFOD project after actively creeping zones were discovered in the SAFOD Main Hole in phase II. The two actively creeping strands of the SAF named the Southwest Deforming Zone (SDZ) and Central Deforming Zone (CDZ) were identified within a ~200m-wide low-velocity zone, which is considered to be the SAF damage zone (Zoback et al., 2010, 2011). Our sample was located at the margins of the damage zone marked in Fig. 1a, ~2.5m SW of the actively creeping SDZ strand at 3196.5m, MD. Notwithstanding the low-velocity extent of the damage zone, Bradbury et al. (2011) estimated width of the SAF damage zone to be at least 350m including regions that may not be currently active. Holdsworth et al. (2011) considered the gouge outside the creeping strands to be inactive. Terminus of the SAFOD Main Hole, at true vertical depth of ~2.7km, has registered a temperature of 112±2°C.

Several different intervals from the G24 core section have been sampled and studied by others (e.g. Gratier et al., 2011; Holdsworth et al., 2011, Bradbury et al., 2011, 2015; Moore 2014). This core section was characterized as black cataclasite and ultracataclasite with localized mm to sub-mm pyrite and calcite veins running sub-parallel to cataclastic foliation. The gouge was found to be uniquely rich in carbonaceous phases, suggesting hydrocarbon migration in the gouge, and unusually enriched in disseminated secondary pyrite. Bradbury et al. (2011) showed the disseminated pyrite was present in the SDZ wallrock on both sides, and on the NE side of the CDZ. Bradbury et al. (2011) and Holdsworth et al. (2011) suggested that presence of disseminated pyrite, magnetite, and organic carbon in the wallrocks adjoining SDZ and CDZ may be related to the observed loss of Fe from the actively creeping zones.

3. Methods

The sample billet was impregnated with clear epoxy resin and cut for two parallel petrographic thin sections ~10mm apart (G24a, and G24b) at right angles to foliation to enable characterization of the microstructural change within foliation planes. The section surfaces were machine-polished using 0.05μm silicon particle colloidal suspension and vapor-coated by thin carbon deposit. However, most of the analytical work used section A as the 10mm depth revealed little microstructural change. Deformation microstructures were studied using a Zeiss Supra 35VP high resolution SEM with backscattered electron detector and EDX capabilities. Selecting typical areas for electron microscopy was facilitated by creating reference image mosaics using reflected-light optical microscope where pyrite appeared in sharp contrast against the siliciclastic gouge.

The presence of both deformed and undeformed pyrite in the sample prompted a more focused microstructural and crystallographic characterization of the pyrite phase via SEM-based electron backscatter diffraction (EBSD), analysis. For EBSD the samples were polished on a polyurethane lap for one hour using a suspension of 0.05μm colloidal silicon (SYTONTM™) to remove any surface damage. Samples were given a thin carbon coat prior to EBSD to reduce charging effects and maintain a strong crystallographic signal (Prior et al., 1996). All crystallographic data were collected at the University of Liverpool using a CamScan X500 crystal-probe scanning electron microscope (Bestmann et al., 2003) with a thermionic field emission gun, an accelerating voltage of 20kV and a beam current of ~5nA. This technique has a typical angular resolution of <1° and a spatial resolution of ~0.05μm. All data were processed using the software package CHANNEL5 (Oxford Instruments Limited). Sets of rectilinear maps were collected with a 0.5-1.5 μm sampling spacing. Typically, around 70% of points in the grid were successfully indexed. To improve the completeness of maps and thus obtain better grain size, shape and misorientation statistics, the Tango utility (part of CHANNEL 5 software) was used in a systematic way to interpolate data by growing existing mapped grains to fill the non-indexed areas without introducing artefacts (Barrie et al., 2007; Bestmann et al., 2003). Using this reconstruction method generally improved map coverage to ~ 90%. Tango was then used to define grains based on lattice orientation; to investigate lattice misorientation data for visualization of Euler-angle maps and grain-boundary misorientation; to produce band contrast (BC) images from the contrast between diffraction bands and background; and to produce data subsets for plotting misorientation histograms and plotting pole figures (using Mambo). A discussion of the systematic errors in EBSD data collection process, directly applicable to this study, is presented by Prior et al. (1996) and Barrie et al. (2007).

We used Cathodoluminescence (CL) images and spectral color variations of calcite vein networks in the sample to better understand the origin and relative order of the calcite veining and its correlation with pyrite deformation obtained from the EBSD data. The CL images were acquired optically using a CITL-Mk5 cold CL stage system and exposure time between 0.5 and 10 seconds to maximise dynamic range in the acquired image. Since the calcite vein network mostly consisted of vein-saturated clasts and narrow 50-150 μm wide individual veins in the gouge matrix, the spectral analyser in the instrument could not provide uniformly reliable results. Instead, we estimated the spectral values for CL colors of distinct vein generations by a digital color-sampling method: A high-resolution strip image of standard visible-light spectrum (350-750nm band measuring 3500 × 646 pixels currently available from NASA.gov, or Wikimedia.org) was calibrated using the graduated 1964 CIE color space such that 8.75 pixels on the spectrum band represented ~1nm of wavelength on the color space. Image processing software Sigma Scan Pro© v.5 was then used to acquire several multi-pixel color samples from uniformly-colored regions of each distinct calcite vein on CL images. Upon zooming, the color samples yielded small (100-400 square pixel) apparently mono-color areas, which was reshaped into a slender bar measuring ~8.75 × 646 pixels for use with the calibrated chart. The color sample bar was moved against the graduated chart until it became indistinguishable from the chart color within a very narrow range of wavelengths. At this sampling scale, the color samples were mostly mono-color, but occasionally included pixels of a different color. In all measurements, however, a color sample matched the chart colors if it was moved back and forth within a 25 pixel band (~3nm) in the calibrated chart, which gave a ±3nm accuracy for the wavelength estimates.

4. Results

4.1 Microstructures and general compositional observations

The gouge retains a well-defined shape-preferred orientation (SPO) foliation in a clast-in-matrix microstructure (Fig. 2a-b), where large fragments in the gouge consist of extensively fractured and veined elongate sandstone and arkosic siltstone clasts (long axis ~200μm to a few mm). Some of the clasts are cemented aggregates of reworked and intricately veined quartz-rich fragments (Fig. 2c). Similar microstructural features in this and other gouge samples from the SAFOD damage zone cores have been noted and described (e.g. Holdsworth et al. 2011, Bradbury et al. 2011, Richard et al. 2014). The clasts commonly host a network of calcite fracture-sealing veins that generally run at large angles to the clast length (Fig. 2c). It has been shown that in-clast calcite veins in samples from G24 core section, including our sample, resulted from sealing of fractures that propagated from grain contact impingement points at high angles to pressure solution seams (Gratier et al., 2011; Hadizadeh et al., 2012). The pervasive presence of this vein fabric suggests that the gouge foliation (dashed line S in Fig. 2) is a pressure solution cleavage. Evidence of pressure solution in the studied sample is in agreement with previous studies of the damage zone rocks exposed in Holes E and G (Schleicher 2009a; Holdsworth et al 2011; Hadizadeh et al. 2012; Richard et al. 2014; Bradbury et al. 2011, 2015). The gouge matrix comprises shale and clay-rich alteration products of highly comminuted rock fragments (mainly quartz and feldspars). In contrast to calcite veins in the clasts, the calcite veins in the matrix generally run parallel to foliation (Fig. 2a-c). Pyrite in the sample appears as framboids, polycrystalline blocks and stretched clusters.

Pyrite framboids appearing within and around the clasts in Fig. 3 are presumed to be the primary diagenetic pyrite in the fault zone protolith (Sawlowicz 1993; Rickard 1970). The disseminated pyrite similar to those shown in Fig. 3 was described by Holdsworth et al. (2011) as relatively late-stage authigenic pyrite. We do not find direct evidence of relationship between this primary pyrite and the polycrystalline pyrite associated with calcite veins in our sample. It is likely that the polycrystalline pyrite in the gouge is a byproduct of secondary epigenetic mineralization from hydrothermal fluid-rock interactions as HS^- -bearing H_2O-CO_2 fluids were focused in the SAF (Menzies et al. 2016). Mittempergher et al. (2011) reported the presence of anhydrite (CaSO4) veins in the SAFOD damage zone samples. Experimental work has shown pyrite could form at $T>200$°C via reduction of anhydrite in a hydrothermal environment (Graham and Ohmoto 1994). Most relevant to this study, however, is the deformation of the secondary pyrite (hereafter simply referred to as the pyrite, unless otherwise is stated) and its implications for the deformation mechanisms of creep in the SAF at elevated temperatures. As shown in Figs. 2a and 2b, the bulk of the polycrystalline pyrite in the sample appears in two different microstructures: A sigmoidal-block (8×5 mm) and an elongate ~3.5mm long cluster varying in width from 100 to 500μm (Fe-map inset in Fig. 2b). These microstructures suggest a range of formation and deformation conditions for the pyrite. The sigmoidal-block pyrite consists almost entirely of xenomorphic polycrystalline pyrite with no other sulfide minerals present (Fig. 4a). Clear evidence of deformation by brittle fracturing exists as well as brittle attrition at contacts with the gouge matrix (Fig. 4b). The block is smeared out along the foliation in a σ-type kinematic indicator, where the smear consists of comminuted pyrite crystals (Fig. 4c) stretched out along the foliation. The elongate-cluster-pyrite and its margins (Fig. 5) record a different type of deformation and growth relationship (Fig. 5) than the passive brittle attrition observed in the sigmoid-block pyrite. Notable microstructural features at the margins of the elongate-cluster-pyrite include pyrite crosscutting calcite veins (Fig. 5a-c) and implosion microbreccia with pyrite-sealed jigsaw texture (Fig. 5d).

4.2 The Cathodoluminescence of calcite veins

Calcite vein networks in the sample targeted for the Cathodoluminescence (CL) study were found in three categories of microstructures, namely: clasts of different size and vein density (labelled C and SC), veins in clay-rich matrix surrounding the clasts (labelled M), and the gouge regions where pyrite crosscuts the calcite veins (labelled P in Fig. 6a). The large siltstone clast (SC) in the sample (Fig. 6a) is less densely pervaded by calcite veins than the, smaller, quartz-rich clasts (C). Instrument-output CL images for the representative microstructures are shown in labelled boxes in Fig. 6b. We note that CL imaging was carried out at five location in one siltstone clast (SC1 through SC5), but only two representative images (SC1 and SC2) are displayed in Fig.6b. They are representative because the calcite-vein luminescence characteristics showed little variability over the entire clast. The CL data for calcite veins in the gouge matrix (M) were collected from the veins marked in Fig. 6b-C2 and C4 (solid white arrows). Except for fracture-sealing calcite in the pyrite block (Fig. 6b-P2), which we regarded as a matrix vein, all other matrix veins were found to be sub-parallel to the trace of the foliation.

In general, luminescence images of the vein-calcite tend to change from dark red (679nm-e.g. SC1, SC2 in Fig. 6b) to a bright red-orange color (588nm-e.g. vein marked M, in Fig. 6b-C2). The luminescence range, however, includes two distinct step-downs between the maximum and minimum wavelength values as presented in a box-whisker plot of luminescence wavelengths based on 78 spectral measurements (Fig. 7). The plot reveals a significant difference in median wavelength values between the large siltstone clast (672nm) and a group of microstructures consisting of smaller quartz-rich clasts and the veins crosscut by the pyrite (622nm). The decrease in median wavelength value for the matrix veins relative to the smaller clasts group appears to be transitional as indicated by the fitted curve in Fig. 7. The EDX spot analysis showed combined Fe + Mn + Mg elemental concentrations of ~1 wt.%, ranging from 0.31-1.63 wt.% in the typical calcite vein composition. The results plotted in a ternary diagram (Fig. 8) indicate that calcite veins with dull luminescence have high mean atomic wt.% concentration of Fe (0.44) with lower concentrations for Mn (0.34), and Mg (0.23). The bright veins, on the other hand, have high mean atomic wt.% concentration of Mn (0.67) with lower concentrations for Fe (0.23) and Mg (0.11). The mean atomic wt.% concentrations for the medium luminescence veins also have high mean atomic wt.% concentrations of Mn (0.44) with lower Fe (0.3) and Mg (0.15). Correlation of the calcite luminescence color and ternary distribution of these elements as indicated in Fig. 8 is consistent with previous findings that suggest Fe acts as a quenching agent in calcite luminescence (Machel 2000).

4.3 EBSD ***

The results of Electron Backscattered Diffraction (EBSD) study of the sample concentrate on pyrite and are presented as Euler-angle maps with grain boundaries classified by misorientation angle, misorientation histograms and profiles, and pole figures. The sigmoidal-block pyrite and elongate-cluster pyrite microstructures are of particular interest because they texturally interact with the calcite vein networks and matrix of the gouge (Figs. 2-5).

Figure 9 contains two Euler-angle maps summarising EBSD-derived relationships in part of the sigmoidal-block pyrite located in Fig. 4a. Fig. 9a is an 800×500 μm area analysed at 1 μm step size, which shows the pyrite aggregate has undergone brittle deformation including a curved thoroughgoing microfracture and a 100 μm wide zone of attrition breccia. Fig. 9c is a 180×135 μm sub area of Fig. 9a analysed at a 0.2 μm step size. Grain sizes are typically <5 μm up to ~100 μm. The wide Euler-angle color variations between pyrite grains in Figures 9a and 9c reflect the absence of any significant crystallographic preferred orientation (CPO) in the pyrite aggregate, which is typical due to the cubic symmetry of pyrite (Barrie et al., 2007). The grain-boundary colors indicate a significant number of low-angle misorientations: white (1-2°) and yellow (2-5°) boundaries. The same excess of low-angle boundaries is summarised in the misorientation histograms in Figures 9b and 9f. The random-pair (uncorrelated) histograms correspond closely to the theoretical random distribution, which is common in many cases of massive sulphide-ore pyrite deformation (Barrie et al., 2010a; Barrie et al., 2010b; Barrie et al., 2007; Boyle et al., 1998). On the other hand, the neighbour-pair (correlated) misorientation distributions differ significantly from the theoretical random distribution confirming the development of low-angle grain boundaries. On the basis of grain boundaries being defined by a 2° misorientation, about 8% of the 8,714 pyrite grains identified in Figure 9a have a mean internal misorientation of 1° or greater, with a maximum mean internal misorientation of 6.5°.

The higher resolution analysis shown in Fig. 9c illustrates a microstructure where some larger grains of pyrite are mantled by smaller grains of pyrite. Two misorientation profiles across one of the larger grains and the adjacent smaller grains in Fig. 9d indicate the development of a core and mantle relationship (Urai et al., 1986), with the small grains having progressively rotated lattice orientations relative to the large core pyrite grain. Pole figures in Fig. 9e summarise lattice orientations in three of the larger grains in Fig. 9c. The large central pale-blue-colored grain (i) shows a dispersion of <100> and <110> orientations with no systematic rotation around any particular pyrite crystallographic axis. The upper large purple-colored grain (ii) in Fig. 9c has developed a low-angle grain boundary to form two main sub-grains misoriented by a rotation about the near-vertical <110> axis in Fig. 9e (ii). The area (iii) in Fig. 9c consists of two grains sharing a high angle (>25°) boundary. However, given the nature of deformation in the neighbouring grains (i) and (ii), and lattice rotation about a common <100> axis (Fig. 9c, pole figure for iii) we infer that the two grains in (iii) were part of a single large grain. The alternative interpretation is that the common <100> direction is purely coincidental.

The EBSD results from a part of the sigmoidal-block pyrite strongly affected by calcite-sealed brittle fracturing are presented in Fig. 10. The Euler-angle map (Fig. 10b) shows most pyrite grains are <10μm in size, ranging up to ~100μm, and low-angle sub-grains with misorientation boundaries ≤5° are abundant (boundaries mapped in white and yellow in Fig 10b). The misorientation histogram of the map area in Fig. 10c reveals that uncorrelated grains have a misorientation-angle distribution close to the expected theoretical distribution for randomly oriented pyrite grains. In contrast, the correlated misorientation angle distribution (pairs of grains with a mutual grain boundary) in Fig. 10c differs markedly from the expected theoretical distribution, most notably by having an excess of low angle misorientation boundaries. This distribution is simply a reflection of the abundant low-angle boundaries mapped in Fig. 10b indicating the development of pyrite sub-grains.

Moving on to the elongate-cluster pyrite (referenced in Figs. 2a and 5c), the X-ray element map in Fig. 11a, the CL image in Fig, 11c, and the BSE image in Fig. 11d clearly show pyrite-growth microstructures continue out from margins of the elongate-cluster pyrite to crosscut both quartz clasts and calcite veins. The Euler angle map (Fig. 11b) shows that the core of the elongate cluster consists of fine-grained (mostly <5 μm) polycrystalline pyrite with abundant low-angle misorientation boundaries (mapped white and yellow), confirmed by the misorientation histogram in Fig. 11g. In contrast, the microstructures at the elongate-cluster margins comprise relatively large grains with locally idiomorphic outlines and little or no internal microstructure. Figs. 11e and 11f show misorientation angle profiles for the 6 EBSD transects in Fig. 11b. Profile 1 (Fig. 11e-1) demonstrates sub-grain development in one of the larger elongate-cluster core grains, whereas Profile 2 (Fig. 11e-2) demonstrates no measurable internal strain (total angle change of <1°) in a marginal idiomorphic pyrite grain that cross-cuts calcite veins in the adjacent quartz. Profile 3 (Fig. 11e-3) crosses a large (<200 μm) pyrite grain adjacent to the elongate cluster. The pyrite grain contains calcite inclusions with similar CL colouring to the calcite veins that cut the adjacent quartz. The profile indicates the development of a low-angle misorientation boundary and little or no other measurable microstructure. Profile 4 (Fig. 11e-4) is across another pyrite grain adjacent to the elongate cluster. This small grain cuts calcite veins in the quartz and records evidence of significant internal misorientation. Profile 5 (Fig. 11f-5) illustrates progressive misorientation and the development of Dauphiné twins in a large quartz clast bordered by calcite veins. Profile 6 (Fig. 11f-6) shows that quartz cataclasite fragments, cemented by calcite veins, are separated by sub-grain boundaries with misorientation angles mostly ranging from 2-10°. The central region of the pyrite-sealed implosion microbreccia (see SEM image of Fig. 5d) was selected for the EBSD analysis in Fig. 12. An X-ray element map shown in Fig. 12b reveals distribution of S, Si and K and resolves the compositional make-up of the area in Fig. 12a. The 0.6μm step-size Euler map (Fig. 12c) and misorientation profile (Fig. 12d) of the pyrite sealing the breccia indicate it is a single crystal with a cumulative lattice misorientation of ~3° across ~80μm profile length.

5. Discussion and conclusions

5.1 What do SAFOD damage zone rocks represent?

It is debatable whether the damage zone rocks bordering CDZ and SDZ are relicts of locked section of the SAF to the south, or they represent uplifted deeper sections of the currently creeping segment of the fault. The answer to this question seems to depend on the overall trajectory of the N-NW-moving block of the SAF as well as interactions of the block with the entrained serpentinite bodies on the E-NE block of the fault. The horizontal component of the trajectory for the last 1-2 million years involves ~30km strike-parallel displacement between the locked-to-creeping transition boundary at Cholame, SE of Parkfield and position of SAFOD drill site. Assuming E-NE block of the SAF stationary, at a displacement rate of ~30mm/year, it would take the locked section rocks ~1 million years to be placed at SAFOD site. Although the creeping section of the SAF in central California has been the subject of numerous geophysical and geotectonics studies (e.g. Wang et al. 1984; Montgomery 1993; Page et al. 1998; Townend and Zoback 2004; Rolandone et al. 2008; Blythe et al. 2004; Titus et al. 2007 and 2011), the uplift component of the trajectory remains uncertain. Based on fission-track data from the SAFOD pilot hole, Blythe et al. (2004) estimated that the site had experienced ~1 km of uplift in the past 4-8 million years. Schleicher et al. (2009) estimated a temperature of 200°C for the formation of phyllosilicates (illite-smectite) from the bottom of the Main Hole. At 35°C/km gradient, this would represent an uplift of ~2.5 km. It is not clear how much of this uplift could predate faulting. Based on sedimentary basin temperature profiles, Moore (2014) estimated the upper and lower temperature limits for saponite-to-corrensite transition respectively at 225°C and 125°C and suggested that the lower limit requires ~0.5 km uplift of the SDZ rocks. She suggested that the cooling might have resulted from up-dip movement of low-density material in the active bands relative to the damage zone rocks. However, the net uplift estimates are further complicated by the buoyancy-driven up-dip movement of low-density bodies of gouge within the entire damage zone of the SAF (Wang 1984). With respect to the latter point, it is important to note that mineral signatures of serpentinite alteration (e.g. chrysotile, lizardite, and smectite clays as well as chromium oxide and magnetite) are present in the damage zone rocks (Fig. 3, Bradbury et al. 2012). Thus, emerges a very gently uplifting N-NW-directed displacement trajectory for the quartzofeldspathic rocks, which are likely to include strands/pods of the clay-rich gouges progressively generated through displacement as well as hydrothermal reactions with the entrained serpentinite bodies (Moore and Rymer 2012). We, therefore, propose that the damage-zone rocks encountered in the SAFOD have an interlaced structure consisting of the SAF locked-section relicts as well as clay-rich gouge that represents deeper sections of the creeping segment of the fault.

5.2 Analysis of sample results

We identified two distinct generations of calcite veins. The veins in the survivor/reworked clasts were generally perpendicular to enclosing foliation (Fig. 2), which allowed us to define the foliation as pressure solution cleavage. We also noted calcite veins sub-parallel to foliation (white arrows in Fig. 2c) and calcite-sealed late fractures in the block pyrite (Fig. 4 and Fig. 6-P2). The CL results enabled us to resolve the two vein generations in terms of relative depth of crystallization (P1 and P2 in Fig. 13). Studies of calcite from different geological environments have attributed the CL sequence non-luminescent, bright, and dull emission in calcite to a progressive decrease in the oxidation state of the pore water and, therefore, deeper environments during crustal burial (Grover and Read 1983; Machel et al. 1985; McManus and Wallace 1992; Machel 2000; Verhaert et al. 2004). We assume that, at the minimum, the observed luminescence of calcite veins in both clasts and matrix of the gouge (Fig. 6b) suggests a reducing tectonic environment mostly isolated from direct interaction with oxygen-rich meteoric water. The analysis of visible-light wavelengths in the CL images in Fig. 7 indicates that luminescence of the studied calcite veins varies with the type of microstructure they pervade. The wavelength median values (curve fitted to Fig. 7 plot) suggest that veins in the large arkosic siltstone clast (SC boxes in Fig. 6a-b) precipitated at a greater depth relative to the vein-calcite elsewhere in the sample (Fig. 13). The calcite veins from the deepest environment are part of this microstructural record simply because they happened to be in this particular large survivor clast. Thus, in this instance, clast size difference can explain the large difference in CL wavelength between SC veins and other calcite veins in Fig. 7. The lowest luminescence median values in Fig. 7 are from the foliation-parallel matrix veins (marked M in images C2, C4 in Fig. 6b and in Fig. 13), which we consider unrelated to pressure solution cleavage. The CL wavelength plot in Fig. 7 suggests that late fractures in the pyrite sigmoidal block (P2 in Fig. 6b and 13) are sealed with calcite that precipitated at depths equivalent to the bottom of the SAFOD borehole (2-4km). Luminescence of the veins in the highly reworked, quartz-rich clasts thus falls within an intermediate range of depths relative to the end members. The wavelength median value for calcite luminescence in the quartz-rich clasts is ~620nm, which is close to the observed typical calcite CL (Cazenave et al. 2003). We also independently used the trace element proportions in Fig. 8 to check the luminescence results. A highly debated factor affecting the range of luminescence of calcite is the Fe/Mn ratio in the atomic structure of calcite (both elements in ppm concentrations), which also correlates with pore-water chemistry (Barnaby and Rimstidt 1989; Budd et al. 2000; Habermann et al. 2002; Cazenave et al. 2003). In general, increasing Fe tends to suppress (quench) luminescence while Mn acts as an enhancer of the luminescence. The latter effect is demonstrated in Fig. 8 as high wt.% concentrations of Mn in the bright and medium luminescence calcite veins. The highest and lowest Fe/Mn ratios (1.30 and 0.35) occur in the dull and bright luminescence calcite veins, respectively. The change in luminescence of the calcite veins suggests that earliest microstructures in the gouge were deformed at a deeper, more reducing environment (Fig. 13), where more iron atoms were available to be incorporated into the $CaCO_3$ unit cell. The trace element concentration data together with the observed range of calcite vein luminescence, and a fabric defined by the vein network suggest clear evidence of deformation by pressure solution in the gouge that was transported and uplifted to the current position in the SAFOD borehole.

We use the revised pyrite deformation mechanism map published by Barrie et al. (2011) to infer that pyrite should deform by brittle and/or Coble-creep mechanisms under the observed SAFOD P-T-$\dot{e}$ conditions (~3km, ~120°C, and ~10^{-10}/s to ~10^{-12}/s strain rates corresponding to creep rates of ~25 mm/year). While the pyrite deformation involved brittle fracture, the pyrite also deforms by other mechanisms. The sigmoidal block and the main part of the elongate cluster are characterised by small grain-size, distributed misorientations, abundant low-angle boundary misorientations, and subgrain development. Further, the core and mantle relationship in Fig. 9c is consistent with progressive misorientation of the core pyrite and the development of new grains by subgrain rotation recrystallization (SGR) that developed a mortar texture (Urai et al., 1986). A more general occurrence of SGR would be consistent with the observed development of excess low-angle misorientation boundaries in both the sigmoidal block and the elongate cluster microstructures.

The only previously reported case of SGR deformation in pyrite is in Barrie et al. (2007, Figure 15) in a study of the samples experimentally deformed by Cox et al. (1981) at 300 MPa, a strain rate of $2x10^{-4}s^{-1}$, and a range of temperatures from 550°C to 700°C. Subgrain rotation deformation was identified in the samples deformed at 600-650°C, whereas the lower temperature run at 550°C was characterised by bulging deformation, and the 700°C run by complete recrystallization and loss of low-angle boundaries, which is analogous to dislocation creep regimes 1, 2 and 3 of Hirth and Tullis (1992) for quartz aggregates. The lack of widespread development of classic regime 1 bulging and regime 2 SGR microstructures in naturally deformed pyritic ores is probably due to the effects of weaker co-existing minor sulphide minerals such as chalcopyrite, sphalerite and galena that commonly occur in pyrite parageneses (Barrie et al., 2011). Cox et al. (1981) selected a very pure polycrystalline pyrite rock for their experiments, and the sampled SAFOD pyrite aggregates are also very pure without other sulphide minerals. Barrie et al. (2010a, Figure 8) documented evidence of bulging deformation in a pyritic ore from the Godthåp mine in the Røros area of Norway deformed in biotite-zone pelitic rocks during the Caledonian orogeny. The biotite isograd in low to medium pressure metamorphic terrains is generally considered to represent a temperature of at least ~400°C with garnet commonly appearing at ~470-480°C (Ferry, 1984; Wang et al., 1986), bracketing temperature conditions for bulging deformation in pyrite at typical orogenic strain rates. Thus, the SGR deformation microstructure in pyrite aggregates in our sample represents a temperature significantly above 400°C. We therefore argue that the bulk of these sigmoidal block and the elongate cluster pyrite aggregates experienced SGR deformation at a temperature significantly above 400°C (Fig. 13), representing the oldest recorded deformation in these pyrite aggregates.

The side of the elongate-cluster pyrite facing the large siltstone clast boundary (Figs. 2 and 5) is characterised by fringing growth of relatively large, often idiomorphic pyrite grains with little or no internal deformation (Fig. 11). These pyrite grains commonly crosscut calcite filled veins and contain inclusions of calcite with similar CL colour to the vein calcite. In places, the large pyrite grains form the seal to breccia, here interpreted as an implosion breccia (Fig. 12). The EBSD results (Figs. 9-12) thus indicate three contrasting styles of pyrite microstructure in the two clusters: earlier grain cores characterised by SGR deformation and T conditions significantly below the present SAFOD depth (Fig. 13), later fringing growth rims that cut calcite veins and preserve implosion breccias, and finally brittle fractures consistent with present-day SAFOD conditions (calcite veins designated P2 and M in Figs. 6, 7 and 13). This interpretation implies episodic pyrite mineralization at different times over a range of depths prior to late brittle fracturing, and is consistent with the CL results indicating that late brittle fractures in the sigmoidal-block pyrite are sealed by the youngest calcite veins (Fig. 4b and Fig. 6b-P2). Since the sample is only ~2.5m away from the SDZ, the late brittle fractures in the sigmoidal-block pyrite (Fig. 4) could be the result of a local frictional stress transfer from this active shear zone. In the elongate-cluster pyrite, deformation ranges from sub-grain rotation by dislocation creep in the interior (Fig. 11b traverse 1) to almost undeformed idiomorphic crystals at the fringe (Fig. 11b, traverse 2). The calcite veins that formed at depths below the SAFOD (CL results in Fig. 6b-P1) as well as plastically deformed fragments of the quartz cataclasite (Fig. 11b, traverse 5) are crosscut by successive epitaxial growths of the fringe pyrite crystals. The pyrite-sealed implosion microbreccia (Fig. 12a) appears to be a late event in the pyrite crystallization at hydrothermal temperatures (~200°C). The Euler angle map in Fig. 12c shows that the pyrite seal in Fig. 12a is made of a relatively large single crystal with little to no crystal plastic deformation (misorientation profiles in Fig. 12d). The microbreccia is further evidence of episodic nature of hydrothermal events that involves pyrite mineralization in the SAFOD damage zone rocks. It has been successfully argued that such microstructures indicate coseismic events in fault zones (e.g. Sibson 1986; Holdsworth et al. 2011; Bradbury et al. 2011, 2015). Evidence of transient brittle deformation due to local fluid overpressure in samples from the SAFOD damage zone gouge was also reported by Mittempergher et al. (2011). The discussed results are synthesized in Fig. 13, which plots calcite and pyrite microstructure development against depth and temperature.

As discussed in 5.1, the inactive damage zone of the SAF at SAFOD consist of discrete and well-mixed structural and material domains representing both locked and creeping sections of the fault. Our results provided evidence of pressure solution microstructures as well as episodic hydrothermal pyrite mineralization and pyrite sealing in implosion microbreccia. While the secondary pyrite (and anhydrite reported by Mittempergher et al. 2011), is likely to represent microearthquake activity at a range of depths (Jolivet et al. 2015) in the creeping segment, it is possible for the pressure solution cleavage in the damage zone rocks to develop in either creeping or locked section of the SAF at depths >3km. The evidence of pressure solution in SAFOD cores is taken by some previous studies to represent the dominant deformation mechanism of the aseismic creep over the entire seismogenic zone. Gratier et al. (2011) attributed the microseismic activity in a pressure solution regime to cyclical increase in local diffusion distance required for mass transfer from dissolution sites. They suggested that in the SAF creeping section, regularly recurring microearthquakes would be necessary for the pressure solution to operate at displacement rates > 20mm/year and depths >3km. In this case, the cleavage-related calcite veins generated at a range of depths should be found crosscut and disrupted by co-seismic mineralization of that depth range as the fault rocks are uplifted to SAFOD depth. In the view of this study, however, it is also possible that the observed pressure solution microstructures represent interseismic deformation in the locked section of the SAF, having developed prior to juxtaposition against entrained serpentinite bodies in the E-NE block of the fault. Our EBSD results (Fig. 11) support the latter case since we show that multiple episodes of pyrite crystallization and deformation do not crosscut a single generation of the cleavage-related calcite veins as identified by CL. The latter observation implies that the weak-clay frictional deformation mechanism(s) rather than pressure solution creep is likely to be the predominant aseismic creep mechanism at depths below the SAFOD. It is also possible to infer that the repeating microearthquakes in the creeping section may be due to strain accumulation associated with transposed quartz-rich inclusions of the SAF locked section (also see Collettini et al. 2011; Jolivet et al. 2015). It is important to note that similar studies on a larger sample set are needed to confirm or rule out these implications for the deformation behaviour of the creeping section of the SAF. However, this detailed study of a single sample does demonstrate the utility of using combined calcite and pyrite microstructural analysis to elucidate fault history, suggesting the approach should be more widely used.

Acknowledgements

Betty Mariani and Carmel Pinnington are thanked for assistance with setting up and calibrating the Camscan X500 Crystal Probe for EBSD analysis at the University of Liverpool. Josh Hicks is thanked for assistance with optical CL work at the University of Liverpool. We express our gratitude to Diane Moore and Bob Holdsworth for their insightful review comments.

This research was partially supported by the U.S. National Science Foundation grant NSF-EAR-0545472 to J. Hadizadeh.

References

Barnaby, R. J. and Rimstidt, J. D., 1989. Redox conditions of calcite cementation interpreted from Mn and Fe contents of authigenic calcites. Geol. Soc. Amer. Bull. 101, 795-804.

Barrie, C.D., Boyle, A.P., Prior, D.J., 2007. An analysis of the microstructures developed in experimentally deformed polycrystalline pyrite and minor sulfide phases using electron backscatter diffraction. J. Struct. Geol. 29, 1494-1511.

Barrie, C.D., Boyle, A.P., Cox, S.F., Prior, D.J., 2008. Slip systems and critical resolved shear stress in pyrite: an electron backscatter diffraction (EBSD) investigation. Mineral. Mag.72, 1181-1199.

Barrie, C. D., Boyle, A. P., Salter, M., 2009. How low can you go? - Extending downwards the limits of plastic deformation in pyrite. Mineralogical Magazine 73, 895-913.

Barrie, C., Cook, N., Boyle, A., 2010a. Textural variation in the pyrite-rich ore deposits of the Røros district, Trondheim Region, Norway: implications for pyrite deformation mechanisms. Mineral. Deposita 45, 51-68.

Barrie, C.D., Boyle, A.P., Cook, N.J., Prior, D.J., 2010b. Pyrite deformation textures in the massive sulfide ore deposits of the Norwegian Caledonides. Tectonophys. 483, 269-286.

Barrie, C. D., Pearce, M. A., Boyle, A. P., 2011. Reconstructing the pyrite deformation mechanism map. Ore Geology Reviews 39, 265-276.

Bestmann, M. and Prior, D.J., 2003. Intragranular dynamic recrystallization in naturally deformed calcite: diffusion accommodated grain boundary sliding as a result of subgrain rotation recrystallization. J. Struct. Geol. 25, 1597-1613.

Blythe, A. E., d'Alessio, M. A., Burgmann, R. 2004. Constraining the exhumation and burial history of the SAFOD pilot hole with apatite fission track and (U-Th)//He thermochronometry. GRL 31, L15S16, doi:10.1029/2003GL019407.

Bos, B. and Spires, C. J. 2001. Experimental investigation into the microstructural and mechanical evolution of phyllosilicate-bearing fault rock under conditions favouring pressure solution. J. Struct. Geol. 23, 1187-1202.

Bos, B. and Spires, C. J. 2002. Frictional-viscous flow of phyllosilicate-bearing fault rock: Microphysical model and implications for crustal strength profiles. J. Geophys. Res. 107, 2028- 2040, 10.1029/2001JB000301.

Boyle, A. P., Prior, D. J., Banham, M. H., Timms, N. E., 1998. Plastic deformation of metamorphic pyrite: new evidence from electron-backscatter diffraction and forescatter orientation-contrast imaging. Mineralium Deposita 34, 71-81.

Bradbury, K. K., Evans, J. P., Chester, J. S., Chester, F. M., Kirschner, D. L., 2011. Lithology and internal structure of the San Andreas Fault at depth based on characterization of phase 3 whole-rock core in the San Andreas Fault observatory at depth (SAFOD) borehole. EPSL 310, 131-144.

Bradbury, K. K., Davis, C. R., Shervais, J. W., Janecke, S. U., Evans, J. P., 2015. Composition, alteration, and texture of fault-related rocks from SAFOD core and surface outcrop analogs: evidence for deformation processes and fluid-rock interactions. PAGEOPH 172, 1053-1078.

Budd, D., Hammes, U., Ward, W. B., 2000. Cathodoluminescence in calcite cements: New insights on Pb and Zn sensitizing, Mn activation, and Fe quenching at low trace-element concentrations. J. Sed. Res. 70, 217-226.

Carpenter, B. M., Marone, C., Saffer, D. M., 2009. Frictional behavior of materials in the 3D SAFOD volume. GRL 36, L05302.

Carpenter, B. M., Marone, C., Saffer, D. M., 2011. Frictional strength of the San Andreas Fault from laboratory measurements of SAFOD drill samples. Nature Geosci. 4, 251–254.

Carpenter, B.M., Saffer, D. M., Marone, C., 2012. Frictional properties and sliding stability of the San Andreas fault from deep drill core. Geology 40, 759-762.

Carpenter, B. M., Saffer, D. M., Marone, C., 2015. Frictional properties of the active San Andreas Fault at SAFOD: Implications for fault strength and slip behavior. JGR 120, 5273–5289.

Cazenave, S., Chapoulie, R., Villeneuve, G., 2003. Cathodoluminescence of synthetic and natural calcite: the effects of manganese and iron on orange emission. Mineralogy and Petrology 78, 243-253.

Collettini, C., Niemeijer, A., Viti, C., Smith, S. A. F., Marone, C., 2011. Fault structure, frictional properties and mixed-mode fault slip behavior. EPSL 311, 316-327.

Cox, S.F., Etheridge, M.A., Hobbs, B.E., 1981. The experimental ductile deformation of polycrystalline and single- crystal pyrite. Econ. Geol. 76, 2105-2117.

Cox, S.F., 1995. Faulting processes at high fluid pressures: an example of fault valve behavior from the Wattle Gully Fault, Victoria, Australia. J. Geophys. Res. 100, 12,841-812,859.

Ferry, J.M., 1984. A biotite isograd in South-Central Maine, U.S.A.: Mineral reactions, fluid transfer, and heat transfer. J. Petrol. 25, 871-893.

Freitag, K., Boyle, A. P., Nelson, E., Hitzman, M., Churchill, J., Lopez-Pedrosa, M., 2004. The use of electron backscatter diffraction and orientation contrast imaging as tools for sulfide textural studies: example from the Greens Creek deposit (Alaska). Mineralium Deposita 39, 103-113.

French, M. E., Kitajima, H., Chester, J. S., Chester, F. M., Hirose, T., 2014. Displacement and dynamic weakening processes in smectite-rich gouge from the Central Deforming Zone of the San Andreas Fault. J. Geophys. Res. Solid Earth 119, 1777-1802.

French, M. E., Chester, F. M., Chester, J. S., 2015. Micromechanisms of creep in clay-rich gouge from the central deforming zone of the San Andreas Fault, JGR 120, 827-849.

Goldfarb, R. J. and Groves, D. I., 2015. Orogenic gold: Common or evolving fluid and metal sources through time. Lithos 233, 2-26.

Graham, U.M. and Ohmoto, H., 1994. Experimental study of formation mechanisms of hydrothermal pyrite. Geochim. Cosmochim. Acta 58, 2187-2202.

Gratier, J.P., Richard, J., Renard, R., Mittempergher, S., Doan, M.L., Di Toro, G., Hadizadeh, J., Boullier, A.M., 2011. Aseismic sliding of active faults by pressure solution creep: Evidence from the San Andreas Fault Observatory at Depth. Geology, 39, 1131-1134.

Grover, G. Jr. and Read, J. F., 1983. Paleo aquifer and deep burial related cements defined by regional cathodoluminescent patterns, Middle Ordovician carbonates, Virginia. AAPG Bulletin 67, 1275-1303.

Habermann, D., 2002. Quantitative Cathodoluminescence (CL) spectroscopy of minerals: possibilities and limitations. Mineralogy and Petrology 76, 247-259.

Hadizadeh, J., Mittempergher, S., Gratier, J-P., Renard, F., Di Toro, G., Richard, J., Babaie, H. A., 2012. A microstructural study of fault rocks from the SAFOD: Implications for the deformation mechanisms and strength of the creeping segment of the San Andreas Fault. J. Struct. Geol. 42, 246-260.

Hickman, S., Zoback, A., Ellsworth, W., 2004. Introduction to special section: Preparing for the San Andreas Fault Observatory at Depth. GRL 31, L12S01, doi:10.1029/2004GL020688.

Hirth, G, and Tullis, J., 1992. Dislocation creep regimes in quartz aggregates. J. Struct. Geol. 14, 145-159.

Holdsworth, R.E., van Diggelen, E.W.E., de Bresser, J.H.P., Walker, R.J., Bowen, L., 2011. Fault rocks from the SAFOD core samples: implications for weakening at shallow depths along the San Andreas Fault, California. J. Struct. Geol. 33, 132-144.

Janssen, C., Kanitpanyacharoen, W., Wenk, H.-R., Wirth, R., Morales, L., Rybacki, E., Kienast, M., Dresen, G., 2012. Clay fabrics in SAFOD core samples. J. Struct. Geol. 43, 118-127.

Jolivet, R., Simons, M., Agram, P. S., Duputel, Z., Shen, Z.-K., 2015. Aseismic slip and seismogenic coupling along the central San Andreas Fault. GRL 42, 297-306.

Lockner, D. A., Morrow, C., Moore, D., Hickman, S., 2011. Low strength of deep San Andreas Fault gouge from SAFOD core. Nature 472, 82-85.

McClay, K.R., Ellis, P.G., 1983. Deformation and recrystallization of pyrite. Mineral. Mag. 47, 527-538.

McManus, A. and Wallace, M. W., 1992. Age of Mississippi valley-type sulfides determined using Cathodoluminescence cement stratigraphy, Lennard shelf, canning basin, Western Australia. Economic Geology 87, 189-193.

McCuaig, T.C., Kerrich, R., 1998. P-T-t-deformation-fluid characteristics of lode gold deposits: Evidence from alteration systematics. Ore Geol. Rev. 12, 381-453.

Machel, H. G., 1985. Cathodoluminescence in calcite and dolomite and its chemical interpretation. Geoscience Canada 12, 139-147.

Machel, H. G., 2000. Application of Cathodoluminescence to carbonate diagenesis. In: Cathodoluminescence in Geosciences (Editors Pagel M., Barbin V., Blanc P., Ohnenstetter D.), pp. 271-301. Springer-Verlag, Berlin.

Menzies, C.D., Teagle, D.A.H., Niedermann, S., Cox, S.C., Craw, D., Zimmer, M., Cooper, M.J., Erzinger, J., 2016. The fluid budget of a continental plate boundary fault: Quantification from the Alpine Fault, New Zealand. Earth Planet. Sci. Lett. 445, 125-135.

Mittempergher, S., Di Toro, G.D., Gratier, J. P., Hadizadeh, J., Smith, S., 2011. Evidence of transient increases of fluid pressure in SAFOD Phase III Cores. GRL 38, L03301, doi:10.1029/2010GL046129.

Montgomery, D. R., 1993. Compressional uplift in the central California Coast Range. Geology 21, 543-546.

Moore, D. E. and Rymer, M. J., 2007. Talc bearing serpentinite and the creeping section of the San Andreas Fault. Nature 448, 795-797.

Moore, D. E. and Lockner, D. A., 2011. Frictional strengths of talc-serpentine and talc-quartz mixtures. JGR 116, B01403.

Moore, D. E. and Rymer, M.J., 2012. Correlation of clayey gouge in a surface exposure of serpentinite in the San Andreas Fault with gouge from the San Andreas Fault Observatory at Depth (SAFOD). J. Struct. Geol. 38, 51-60.

Moore, D. E. and Lockner, D.A., 2013. Chemical controls on fault behavior: Weakening of serpentinite sheared against quartz-bearing rocks and is significance for fault creep in the San Andreas system. JGR 118, 1-13.

Moore, D. E., 2014. Comparative mineral chemistry and textures of SAFOD fault gouge and damage zone rocks. J. Struct. Geol. 68, 82-96.

Moore, D. E., Lockner, D. A., Hickman, S., 2016. Hydrothermal frictional strengths of rock and mineral samples relevant to the creeping section of the San Andreas Fault. J. Struct. Geol. 89, 153-167.

Morrow, C. A., Lockner, D. A., Moore, D.E., Hickman, S., 2014. Deep permeability of the San Andreas Fault from San Andreas Fault Observatory at Depth (SAFOD) core samples. J. Struct. Geol. 64, 99-114.

Niemeijer, A. R. and Collettini, C., 2014. Frictional Properties of a Low-Angle Normal Fault Under In Situ Conditions: Thermally-Activated Velocity Weakening. PAGEOPH 171, 2641-2664.

Noda, H. and Lapusta, N., 2013. Stable creeping fault segments can become destructive as a result of dynamic weakening. Nature 493, 518-521.

Page, B.M., Thompson, G.A., Coleman, R.G., 1998. Late Cenozoic tectonics of the central and southern Coast Ranges of California. Geol. Soc. Amer. Bull. 110, 846-876.

Prior, D.J., Trimby, P.W., Weber, U.D., Dingley, D.J., 1996. Orientation contrast imaging of microstructures in rocks using forescatter detectors in the scanning electron microscope. Mineral. Mag. 60, 859-869.

Reddy, S., Hough, R., 2013. Microstructural evolution and trace element mobility in Witwatersrand pyrite. Contrib. Mineral. Petrol. 166, 1269-1284.

Richard, J., Gratier, J-P., Doan, M-L., Boullier, A-M., Renard, F., 2014. Rock and mineral transformations in a fault zone leading to permanent creep: Interactions between brittle and viscous mechanisms in the San Andreas Fault. J. Geophys. Res. 119, 8132-8153.

Rickard, D. T., 1970. The origin of framboids. Lithos 3, 269–293.

Rolandone, F., Bürgmann, R., Agnew, D.C., Johanson, I.A., Templeton, D.C., d'Alessio, M.A., Titus, S.J., DeMets, C., and Tikoff, B., 2008. Aseismic slip and fault-normal strain along the central creeping section of the San Andreas fault. Geophys. Res. Lett. 35, L14305, doi: 10.1029/2008GL034437.

Sawlowicz, Z., 1993. Pyrite framboids and their development: a new conceptual mechanism Geol. Rundsch. 82, 148-156.

Schleicher, A. M., Tourscher, S. N., van der Pluijm, B. A., Warr, L. N., 2009a. Constraints on mineralization, fluid-rock interaction, and mass transfer during faulting at 2-3 km depth from the SAFOD drill hole. JGR 114, B04202.

Schleicher, A. M., Warr, L. N., van der Pluijm, B. A., 2009b. On the origin of mixed-layer clay minerals from the San Andreas Fault at 2.5–3 km vertical depth (SAFOD drill hole at Parkfield, California). Contrib. Mineral. Petrol. 157, 173-187.

Schleicher, A.M., van der Pluijm, B.A., Warr, L.M., 2012. Chlorite-smectite clay minerals and fault behavior: New evidence from the San Andreas Fault Observatory at Depth (SAFOD) core. Lithosphere 4, 209-220.

Sibson, R.H., 1981. Fluid flow accompanying faulting: field evidence and models. Earthquake prediction: An international review, 593-603.

Sibson, R. H., 1986. Brecciation processes in fault zones: Inferences from earthquake rupturing. PAGEOPH 124, 159-175.

Sibson, R.H., 1990. Conditions for fault-valve behavior. Deformation mechanisms, rheology and tectonics, 15-28.

Sibson, R.H., 1992. Fault-valve behavior and the hydrostatic-lithostatic fluid pressure interface. Earth Sci. Rev. 32, 141-144.

Sibson, R.H., 1994. Crustal stress, faulting and fluid flow. Geological Society, London, Special Publications 78, 69-84.

Titus, S. J., DeMets, C., and Tikoff, B., 2006. Thirty-Five-Year Creep Rates for the Creeping Segment of the San Andreas Fault and the Effects of the 2004 Parkfield Earthquake: Constraints from Alignment Arrays, Continuous Global Positioning System, and Creepmeters. Bull. Seismolog. Soc. Amer. 96, 250-268.

Titus, S.J., Housen, B., and Tikoff, B., 2007. A kinematic model for the Rinconada fault system in central California based on structural analysis of en-echelon folds and paleomagnetism. J. Struct. Geol. 29, 961 982.

Titus, S. J, Dyson, M., DeMets, C., Tikoff, B., Rolandone, F., Burgmann, R., 2011. Geologic versus geodetic deformation adjacent to the San Andreas fault, central California. GSA Bull. 123, 794-820.

Townend, J., and Zoback, M.D., 2004. Regional tectonic stress near the San Andreas fault in central and southern California. GRL 31, doi: 10.1029/2003GL018918.

Urai, J.L., Means, W.D., Lister, G.S., 1986. Dynamic recrystallization of minerals, in: Hobbs, B.E., Heard, H.C. (Eds.), Mineral and Rock Deformation: Laboratory Studies. AGU, Washington, D. C, pp. 161–199.

Wang, Chi-Yuen, 1984. On the constitution of the San Andreas Fault Zone in central California. J. Geophys. Res. 89, 5858-5866.

Wang, G.F., Banno, S., Takeuchi, K., 1986. Reactions to define the biotite isograd in the Ryoke metamorphic belt, Kii Peninsula, Japan. Contrib. Mineral. Petrol. 93, 9-17.

Warr, L. N., Wojatschke, J., Carpenter, B. M., Marone, C., Schleicher, A. M., van der Pluijm, B. A., 2014. A “slice-and-view” (FIB-SEM) study of clay gouge from the SAFOD creeping section of the San Andreas Fault at ~2.7 km depth. J. Struct. Geol. 69, 234-244.

Verhaert, G., Muchez, P., Sintubin, M., Similox-Tohon, D., Vandycke, S., Keppens, E., Hodge, E. J., Richards, D. A., 2004. Origin of palaeofluids in a normal fault setting in the Aegean region. Geofluids 4, 300-314.

Zoback, M., Hickman, S., Ellsworth, W., 2010. Scientific drilling into the San Andreas fault zone. Eos Transactions AGU, 91(22), 197-199.

Zoback, M., Hickman, S., Ellsworth, W., 2011. Scientific drilling into the San Andreas Fault Zone and an overview of SAFOD's first five years. Sci. Drilling 11, 14-28.

Figure Captions

Figure 1

The SAFOD core sample. (a): Section at ~90° to surface trace of the San Andreas Fault plane in central California, referenced to SAFOD drill site at Middle Mountain as zero distance on x-axis (not shown). Actively creeping strands of the SAF, Southwest Deforming Zone (SDZ) and Central Deforming Zone (CDZ), were cored with the lateral drilled holes (red lines). Small rectangular boxes (E, and G) represent phase III core intervals within the lateral holes. The sample for this study was extracted SW (up-hole) of SDZ between 3192m MD (Measured Depth) and 3196.5m MD. The section diagram is modified after Bradbury et al. (2011). (b): Outer surface of the SAFOD core section splits marked with metric Measured Depths. The white box marks exact location of the sample extracted for use in this study. Light-color discontinuous streaks in the core are strings of siltstone clasts of different sizes. A prominent calcite vein, (arrow in both halves of the core) separates relatively undeformed massive shale on the right from the foliated gouge. Minor tick marks are 3cm apart; core section feet-to-meter conversion difference/small division = -0.96mm.

Figure 2

Reference optical micrographs. (a-b): Sample G24 whole-section cross-polarized light images of thin sections a and b cut parallel to each other ~10mm apart at right angles to foliation (S). Inset boxes labeled on both sections indicate location of images used in other figures. Section G24b (second down) includes inset Fe-map (box with an arrow attached), which highlights location of pyrite elongate clusters streaked against a large siltstone clast. Sigmoid-block pyrite microstructure (labelled pyr) appears in both sections. Note foliation-parallel calcite veins indicated by a white arrow in top section. (c): A close-up plane-polarized light image of the area shown as box c in whole-section G24a image is typical microstructure of the clay-rich gouge. Note large compound clast covering the top portion of the image that consists of heavily veined reworked quartz-rich fragments. White arrows indicate abundance of foliation-parallel calcite veins.

Figure 3

Framboidal pyrite preserved in a large siltstone clast of siltstone-shale ultracataclasite. The main SEM image is the enlarged area shown within dashed line box (see Fig. 2a). The framboids appear to be associated with pores and cavities within the clast but unrelated to the marginal microstructures of an elongate pyrite cluster that borders the clast. Backscattered SEM images.

Figure 4

Cataclasis of polycrystalline sigmoidal-block pyrite (located in Fig 2a). (a): Optical reflected-light image marked with reference boxes for other images. The deformed block pyrite appears with a tail streaking to lower right of the image smeared parallel to foliation S against a large compound clast. (b): BS-SEM close-up image showing intense fracturing of the pyrite (PY) in contact with gouge matrix (cg) as well as calcite-sealed transgranular fractures (cal). Note the extremely fine pyrite particles (white arrow) swirling in the gouge matrix. (c): BS-SEM close-up image from smeared tail of the block pyrite clearly showing cataclastic nature of the pyrite deformation.

Figure 5

Microstructures of polycrystalline elongate-cluster pyrite. (a): Image (located in Fig. 2b) showing part of elongate-cluster pyrite mass and its marginal microstructures grown along preexisting fracture network and clast boundaries, crosscutting calcite veins. Location of Fig. 5b also shown. (b): Close-up of crosscut calcite-veins (cal). (c): Optical reflected-light image showing another example of elongate-cluster pyrite with marginal microstructures in relation to calcite veins. The pyrite growth is in the gouge matrix along boundaries of a large siltstone clast (whole- section reference in Fig 2a). (d): Close-up image showing Jigsaw-puzzle texture in local implosion microbreccia sealed with pyrite (whole-section reference in Fig. 2b).

Figure 6

Cathodoluminescence images of calcite veins in clasts and matrix of the gouge. (a): Whole- section reference image (plane-polarized light) showing areas selected for CL imaging. (b): Collage of the CL images (unmodified microscope output) from common vein-bearing microstructures in the gouge, namely: Large siltstone clast veins SC1 and SC2 representing all SC areas shown in a; Smaller quartz-rich siltstone clasts C1 through C5; Calcite veins in gouge matrix (M, highlighted by white arrows), orientated parallel to foliation (S) shown within C2 and C4; Fracture-seal veins P1 and P2 respectively in fringe-growth and sigmoid-block pyrite microstructures. Note similarity of CL emission color between P2 and M veins. Reference boxes are provided in P1 and P2 for other images.

Figure 7

Spectral data from calcite CL images plotted vs. four different types of vein-bearing microstructures in the gouge (see Fig. 6 caption for descriptions). Number of measurements per image is shown on each box. Boxes indicate the interquartile range of the CL wavelengths for each microstructure type. Line across each box is the median data value, and vertical lines through boxes span the maximum and minimum wavelength values in each type.

Figure 8

A ternary plot of atomic wt.% Mg-Mn-Fe trace concentrations (<1%) for a selection of calcite veins in the sample. A trend exists for lower Fe-Mg content with decreasing brighter luminescence.

Figure 9

EBSD analysis of polycrystalline bulk in sigmoidal-block pyrite. (a): 1.0 µm step-size, Euler-angle map of pyrite aggregate in polished section G24a (see Fig, 4a for location). Different color areas indicate different crystallographic orientations. Different color lines represent variations in lattice misorientation across boundaries identified in the map. The box locates area (c). (b): Misorientation-angle distribution histogram for data in (a). (c): 0.2 micron step-size, Euler-angle map of pyrite aggregate in polished section (upper box in (a)). The lines terminated in circles or triangles represent transects for misorientation profiles in (d). (d): Misorientation-angle profiles for transects located on (c). (e): Three sets of pole figures (i, ii & iii) for large grains located in (c). Circles in (ii) and (iii) denote a lattice deformation rotation axis. (f): Misorientation-angle distribution histogram for data in (c).

Figure 10

EBSD analysis of areas in sigmoidal-block-pyrite with calcite-sealed brittle fractures. (a): Optical reflected-light view of pyrite cataclasis at its border with gouge matrix and calcite-sealed through going fractures (reference box in Fig 4a). Inset box locates area selected for EBSD analysis. (b): Euler angle map revealing sub-grain structure in polycrystalline block pyrite. (c): Misorientation histogram for the entire Euler angle map. A significant tail of correlated boundary pairs indicates strong crystal-plastic deformation by dislocation creep and sub-grain rotation in the fractured block pyrite.

Figure 11

EBSD analysis for elongate-cluster pyrite microstructures crosscutting quartz clasts and calcite veins. (a): EDS X-ray composition map (red=Ca, green=Si, blue=Fe) showing cluster-pyrite mass with respect to calcite veins and quartz cataclasites in gouge (see location for this image in Fig 5c). Inset box shows area selected for EBSD analysis. (b): Euler angle map revealing sub-grain structure in polycrystalline cluster pyrite and in fringing pyrite grains that crosscut gouge microstructures at the cluster margins. Individual pyrite and quartz grains selected for subgrain misorientation transects from typical areas of the map are labeled as 1 to 6. Letter L on transects indicates the left side of misorientation profiles shown in 11e and f. (c): CL image of calcite veins cut by fringing pyrite structures (white lines mark limit of pyrite in (a)). (d): Optical reflected-light image highlighting crosscutting of calcite veins in (a) and (c) by fringing pyrite. (e): Misorientation profiles for elongate-cluster-pyrite mass (transect 1) and pyrite that crosscuts calcite veins and quartz cataclasite (transects 2-4) and. (f): Misorientation profiles for quartz cataclasite (transects 5-6). (g): Misorientation histogram for the entire Euler angle map. A significant tail of correlated boundary pairs indicates strong crystal plastic deformation by dislocation creep and sub-grain rotation in the main part of the elongate-cluster pyrite.

Figure 12

EBSD analysis for the pyrite-sealed implosion microbreccia. (a): Optical reflected-light image showing area of the microbreccia selected for the analysis (reference box in Fig 5d). (b): EDS X-ray map summarizing distribution of S (green), Si (yellow) and K (magenta). The yellow area is quartz, the magenta area is alkali feldspar and the green is pyrite. (c): Euler angle map showing the pyrite seal consists of a single crystal. White line marks location of misorientation profile. (d): Misorientation profile showing weak cumulative lattice misorientation.

Figure 13

Descriptive depth-temperature diagram correlating CL and EBSD results for calcite veins and secondary pyrite microstructures in the studied sample. Depth order of calcite veins is based on relative depth established via CL. Temperature range estimates for calcite veins are constrained by foliation-parallel (M) veins, calcite-sealed fractures in the pyrite (P2), and P1 veins that were crosscut by fringe growth pyrite (around 200°C isotherm). For further information on pyrite deformation see pyrite deformation mechanism map in Barrie et al. (2011). Thermal gradient of 41°C was adopted based on SAFOD temperature at ~2.7km depth.

Fig. 1a

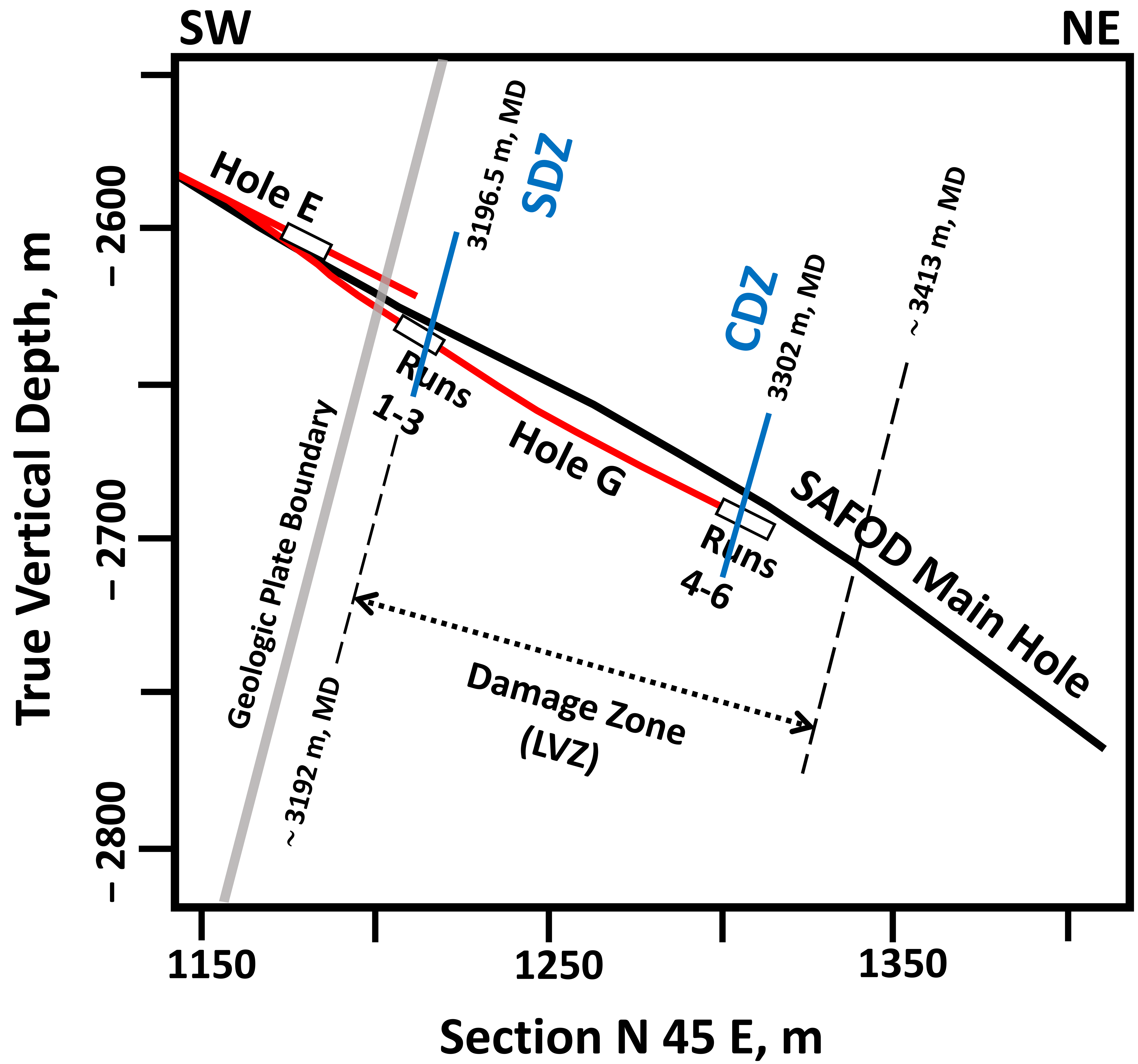

SW
NE
Hole E
Runs 1-3
Hole G
Runs 4-6
SAFOD Main Hole
SDZ
3196.5 m, MD
CDZ
3302 m, MD
~ 3413 m, MD
~ 3192 m, MD
Geologic Plate Boundary
Damage Zone (LVZ)
True Vertical Depth, m
2600
2700
2800
1150
1250
1350
Section N 45 E, m

Fig. 1b

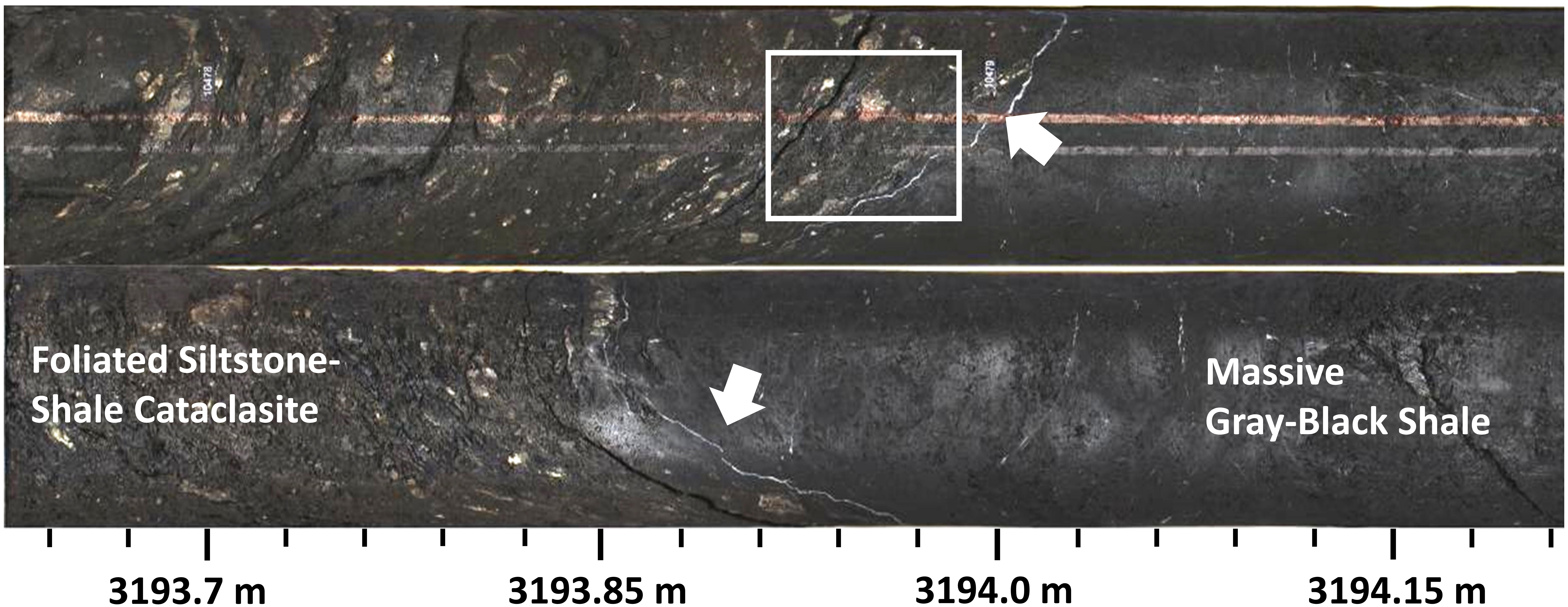
10478
10479
Foliated Siltstone-
Shale Cataclasite
Massive
Gray-Black Shale
3193.7 m
3193.85 m
3194.0 m
3194.15 m

Fig. 2

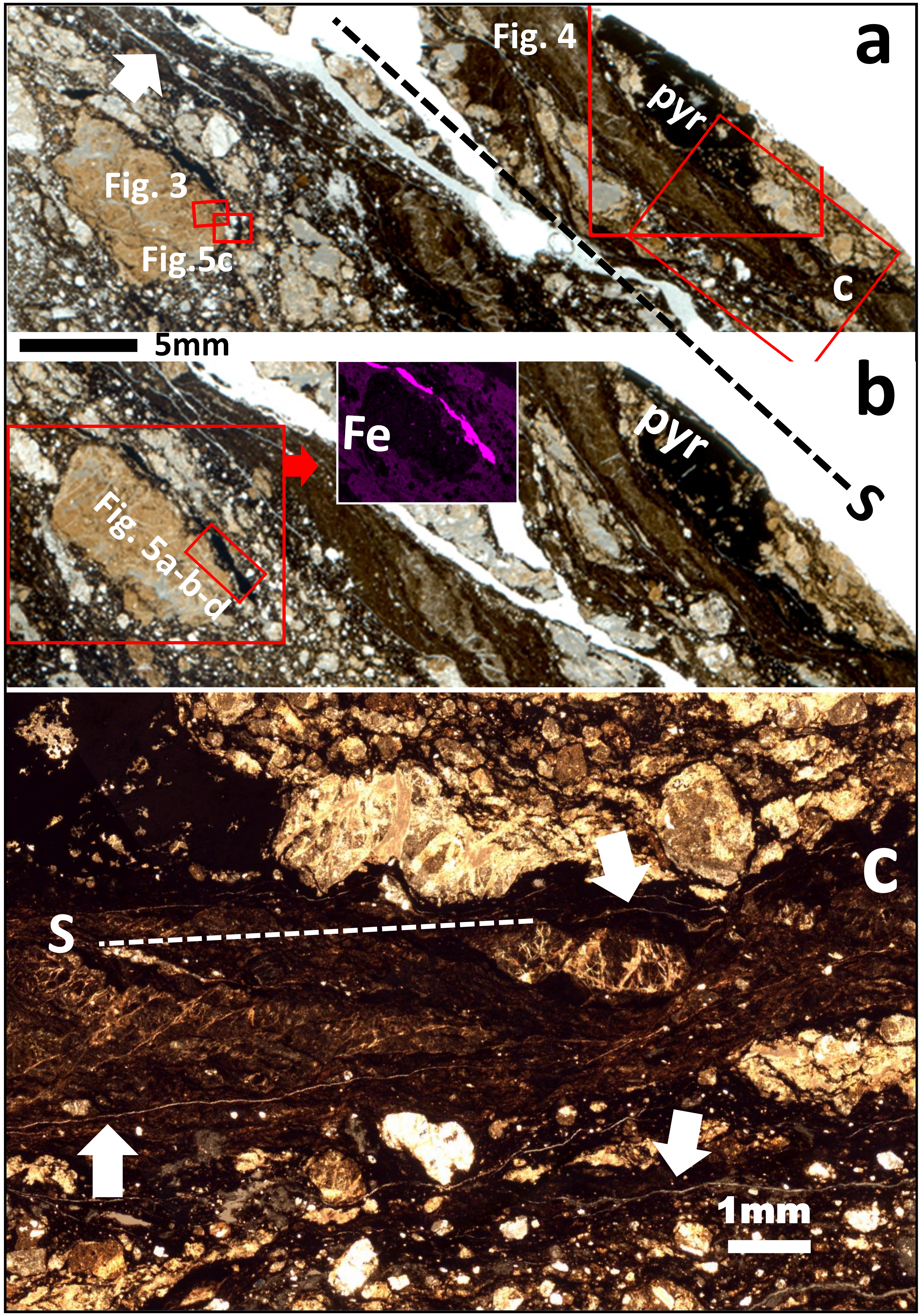

Fig. 3

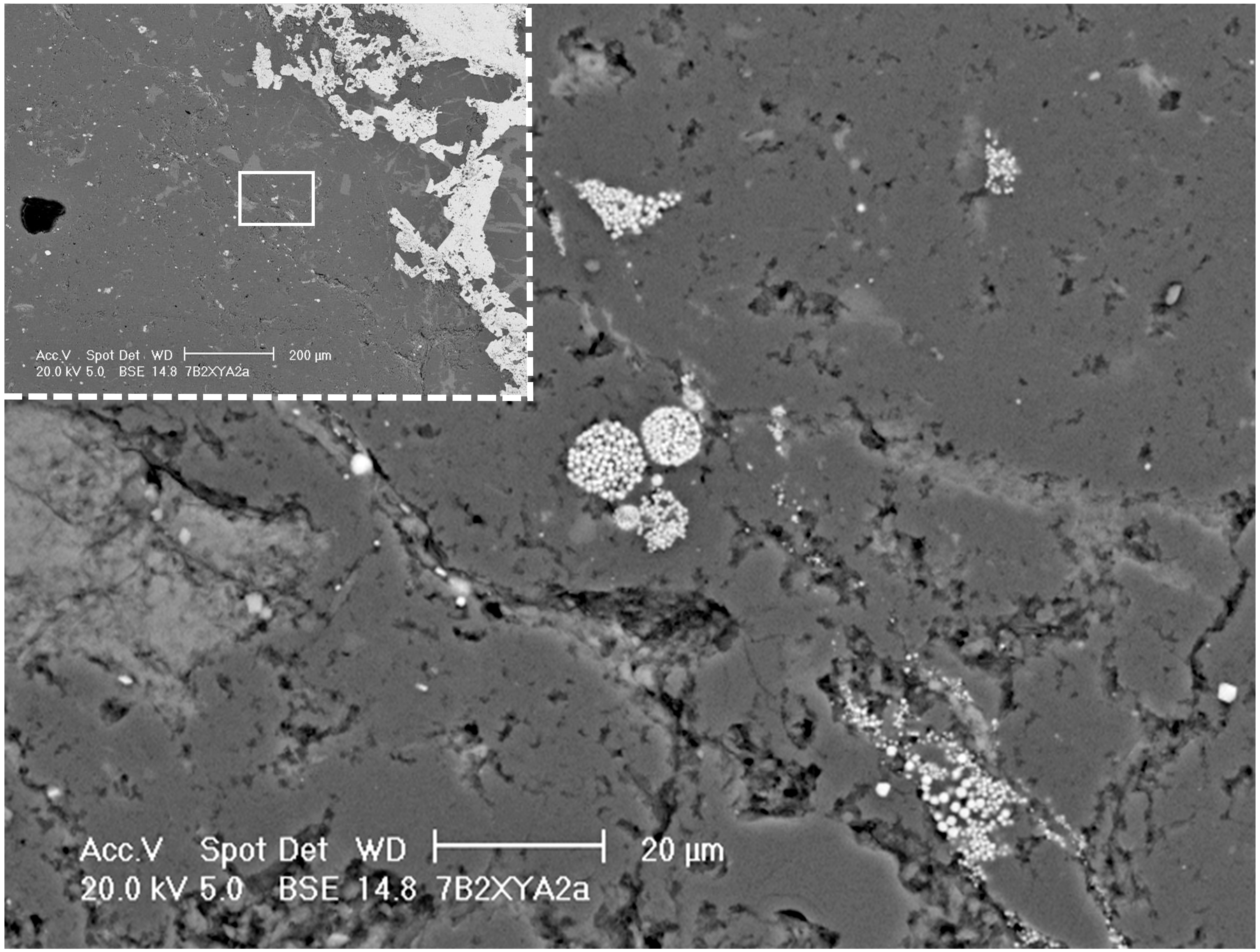
Acc.V Spot Det WD 200 µm
20.0 kV 5.0 BSE 14.8 7B2XYA2a
Acc.V Spot Det WD 20 µm
20.0 kV 5.0 BSE 14.8 7B2XYA2a

Fig. 4

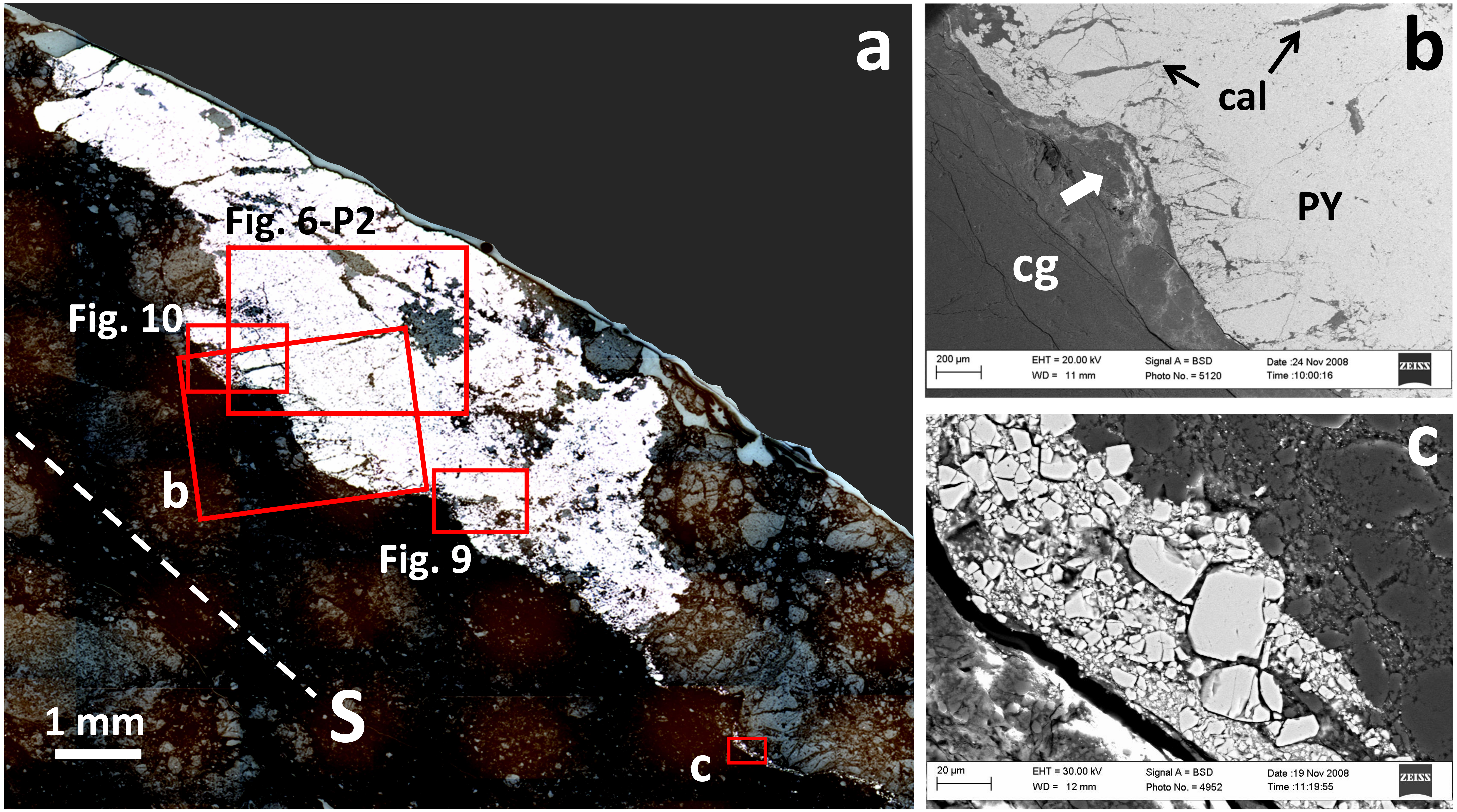

a
Fig. 6-P2
Fig. 10
b
Fig. 9
S
1 mm
c
b
cal
PY
cg
200 µm
EHT = 20.00 kV
WD = 11 mm
Signal A = BSD
Photo No. = 5120
Date :24 Nov 2008
Time :10:00:16
c
20 µm
EHT = 30.00 kV
WD = 12 mm
Signal A = BSD
Photo No. = 4952
Date :19 Nov 2008
Time :11:19:55

Fig. 5

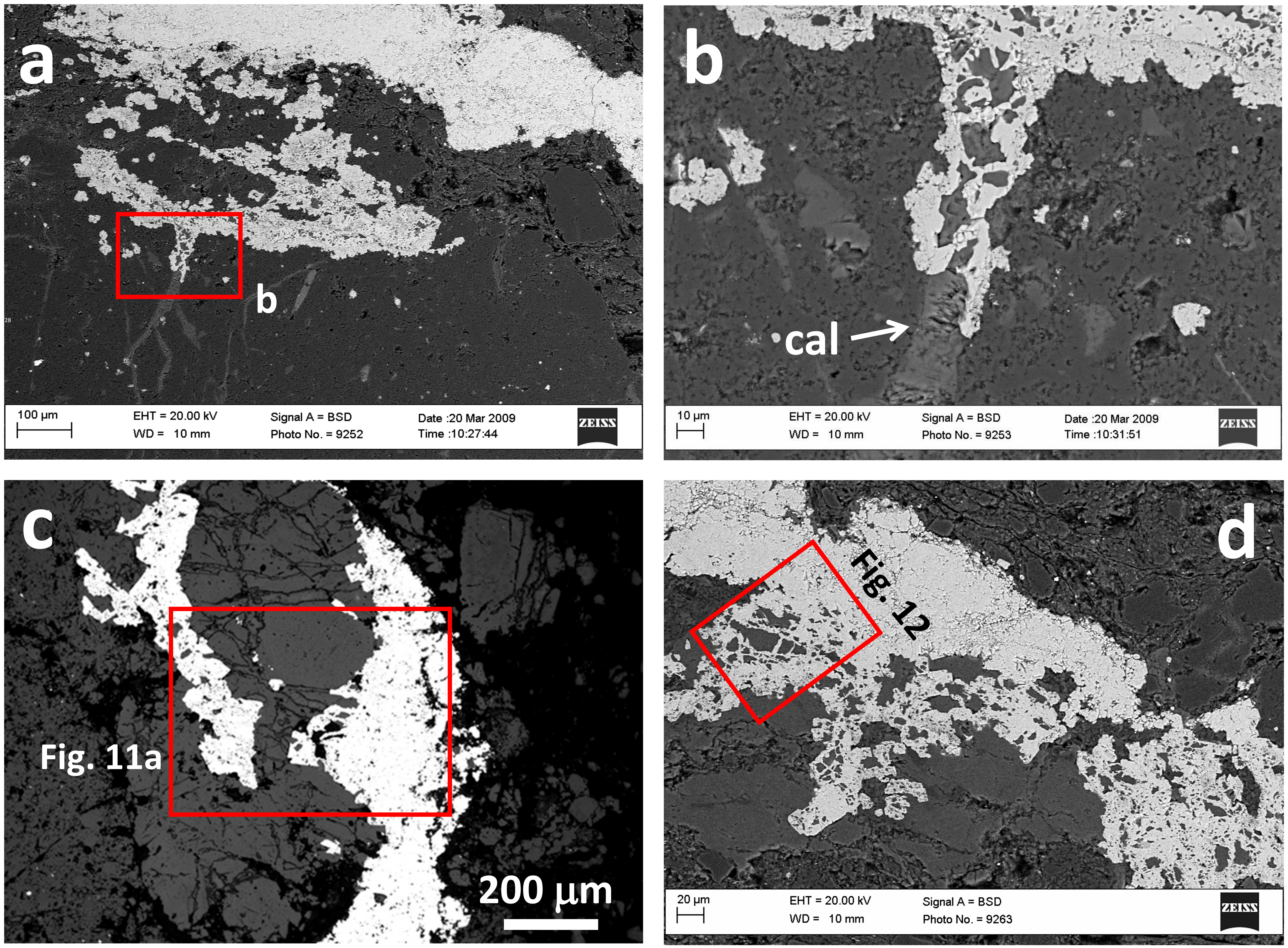

a
b
100 µm
EHT = 20.00 kV
WD = 10 mm
Signal A = BSD
Photo No. = 9252
Date :20 Mar 2009
Time :10:27:44
ZEISS
b
cal
10 µm
EHT = 20.00 kV
WD = 10 mm
Signal A = BSD
Photo No. = 9253
Date :20 Mar 2009
Time :10:31:51
ZEISS
c
Fig. 11a
200 µm
d
Fig. 12
20 µm
EHT = 20.00 kV
WD = 10 mm
Signal A = BSD
Photo No. = 9263
ZEISS

Fig. 6

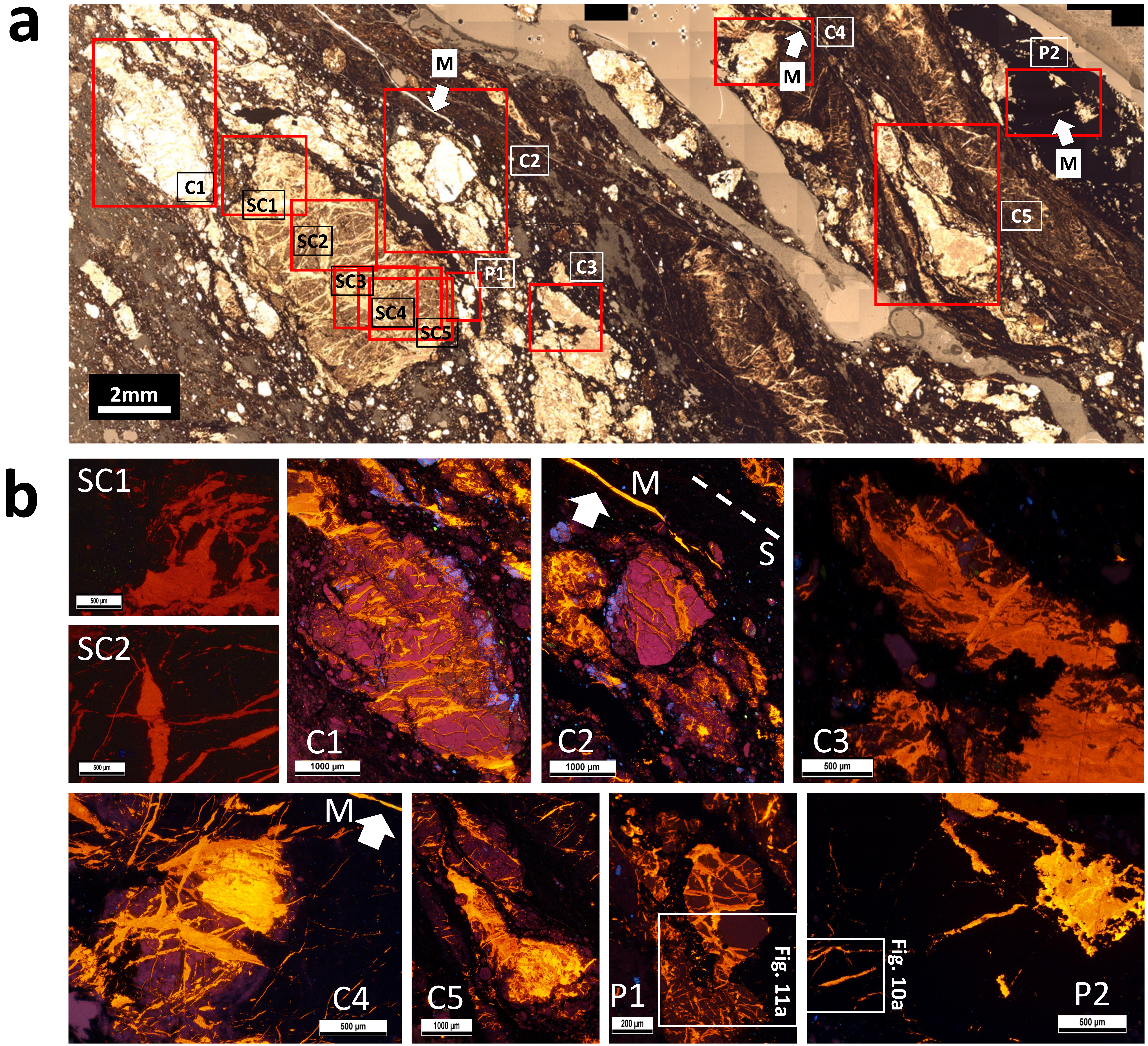

a
M
C4
M
P2
C1
SC1
C2
M
SC2
C5
SC3
P1
C3
SC4
SC5
2mm
b
SC1
500 µm
SC2
500 µm
C1
1000 µm
M
S
C2
1000 µm
C3
500 µm
M
C4
500 µm
C5
1000 µm
P1
200 µm
Fig. 11a
Fig. 10a
P2
500 µm

Fig. 7

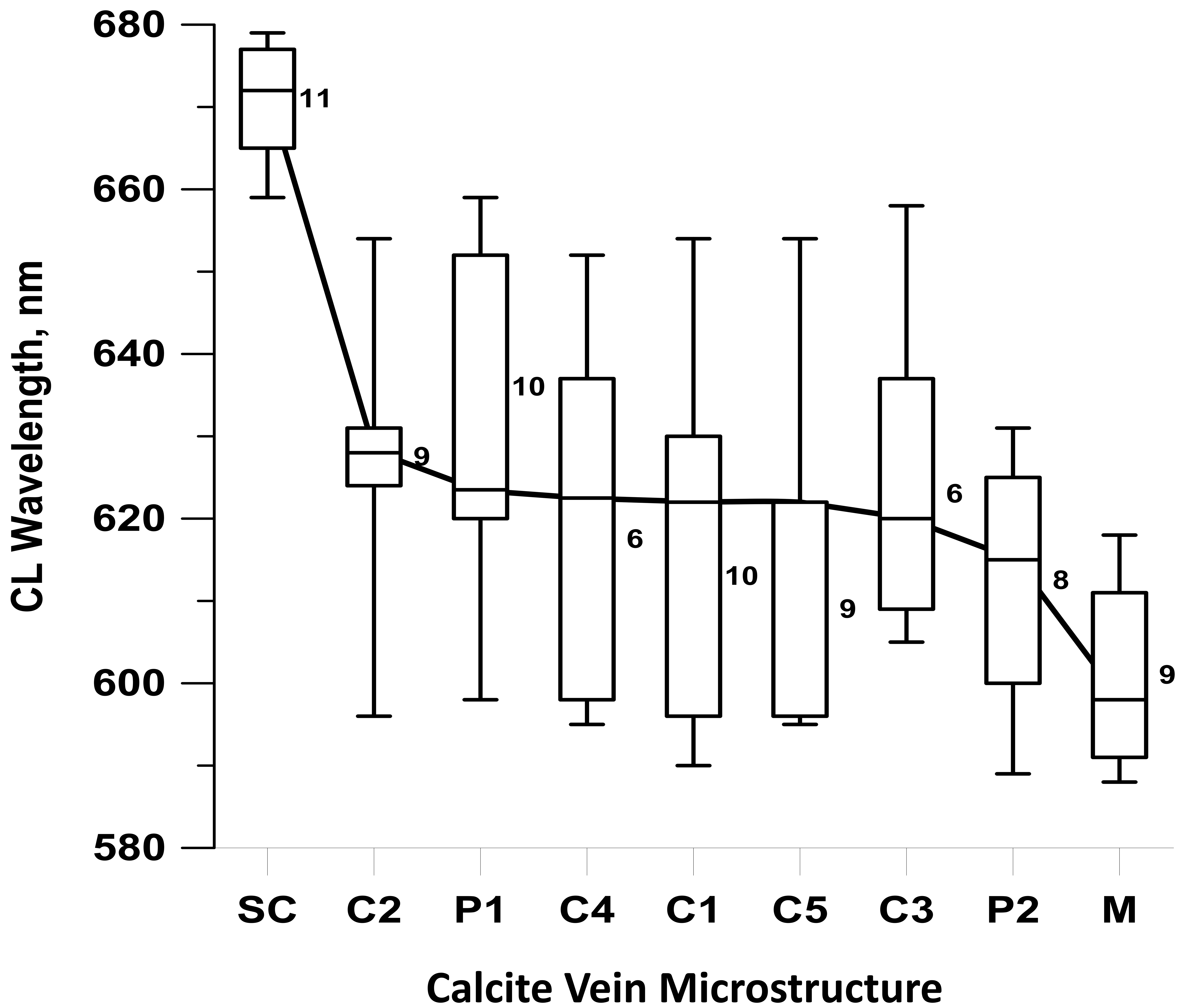

680
660
640
620
600
580
CL Wavelength, nm
11
9
10
6
10
9
6
8
9
SC
C2
P1
C4
C1
C5
C3
P2
M
Calcite Vein Microstructure

Fig. 8

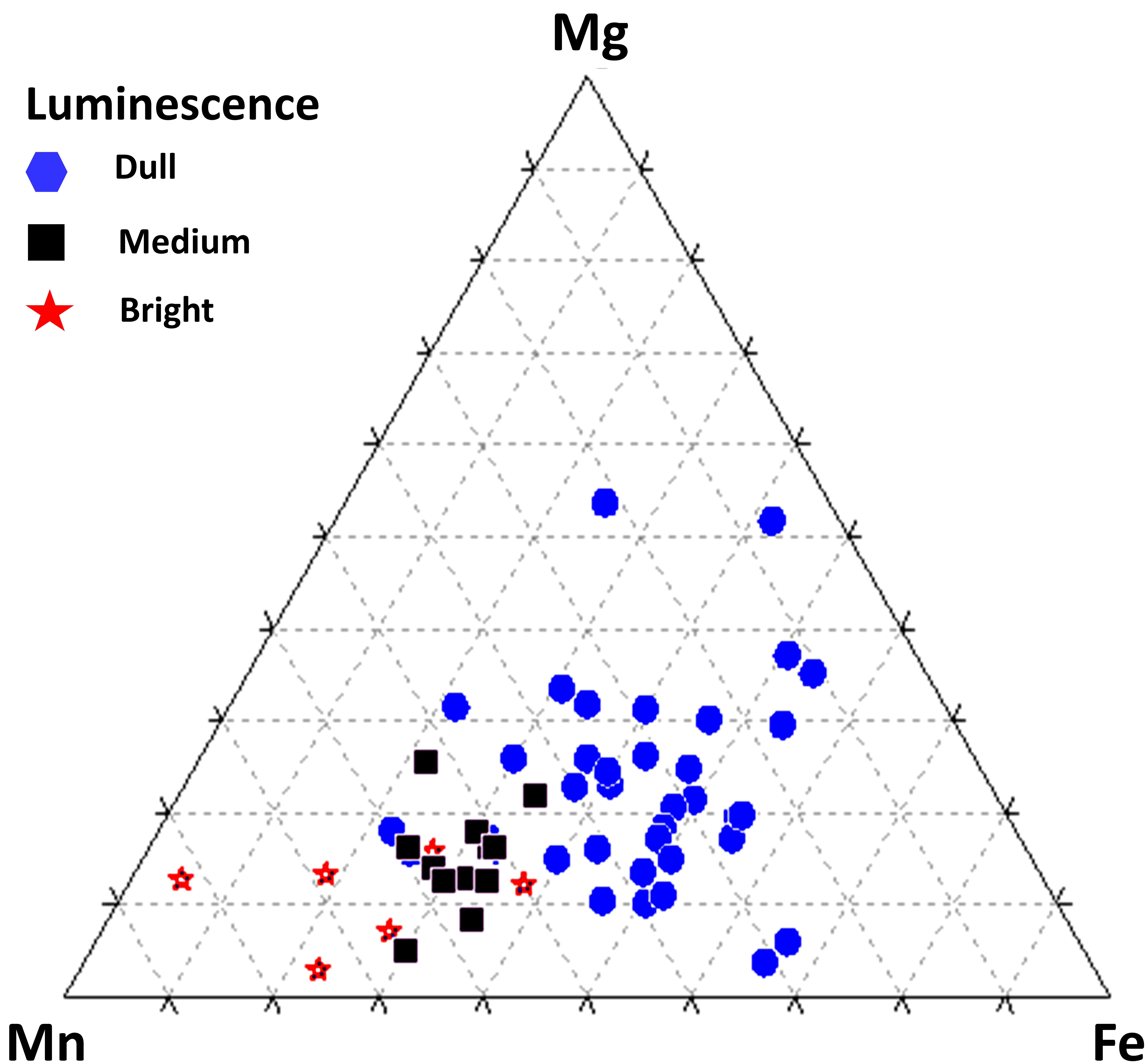

Fig. 9

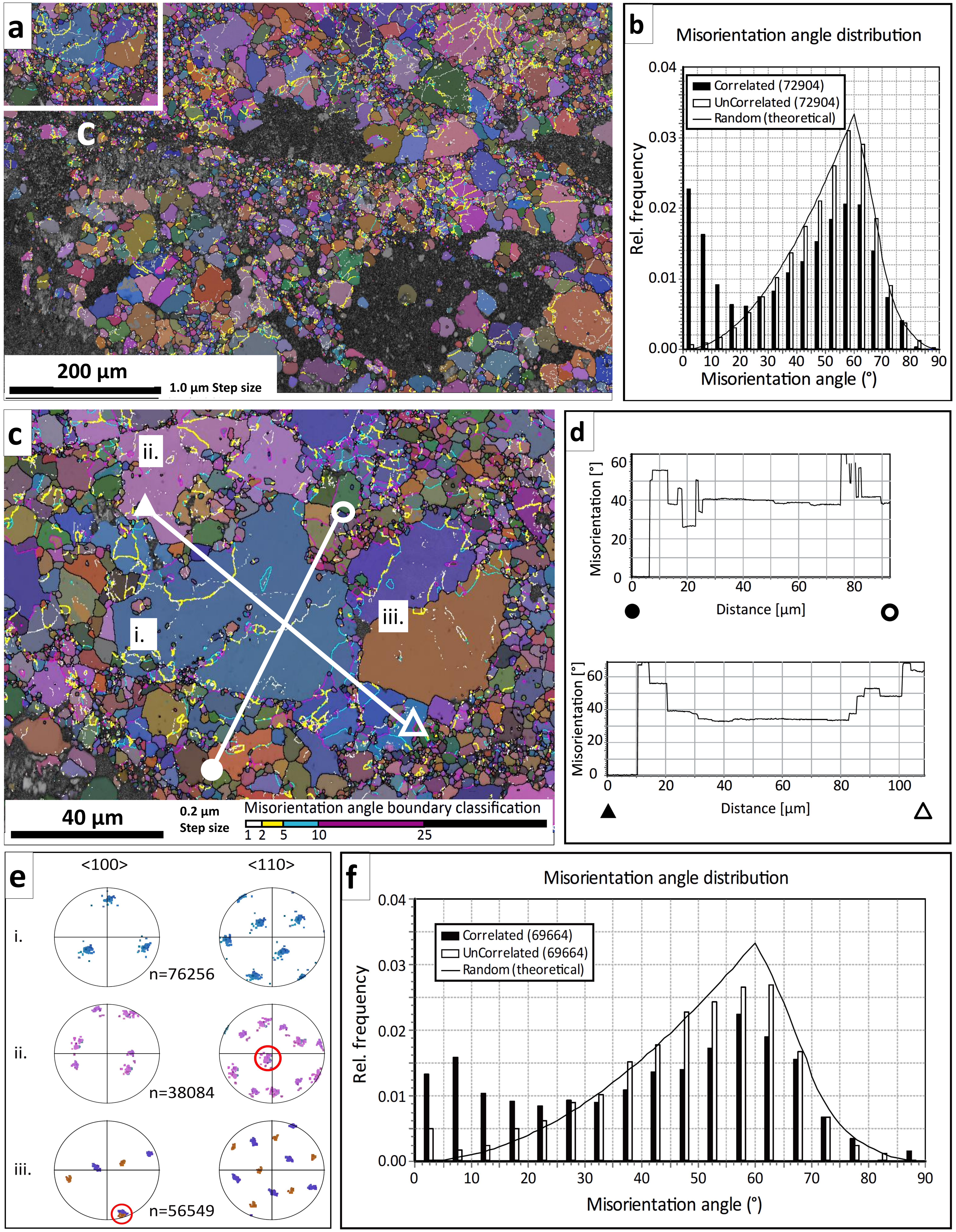

a
c
200 µm
1.0 µm Step size
b
Misorientation angle distribution
Correlated (72904)
UnCorrelated (72904)
Random (theoretical)
Rel. frequency
Misorientation angle (°)
c
ii.
i.
iii.
40 µm
0.2 µm Step size
Misorientation angle boundary classification
1 2 5 10 25
d
Misorientation [°]
Distance [µm]
e
<100>
<110>
n=76256
n=38084
n=56549
f
Misorientation angle distribution
Correlated (69664)
UnCorrelated (69664)
Random (theoretical)
Rel. frequency
Misorientation angle (°)

Fig. 10

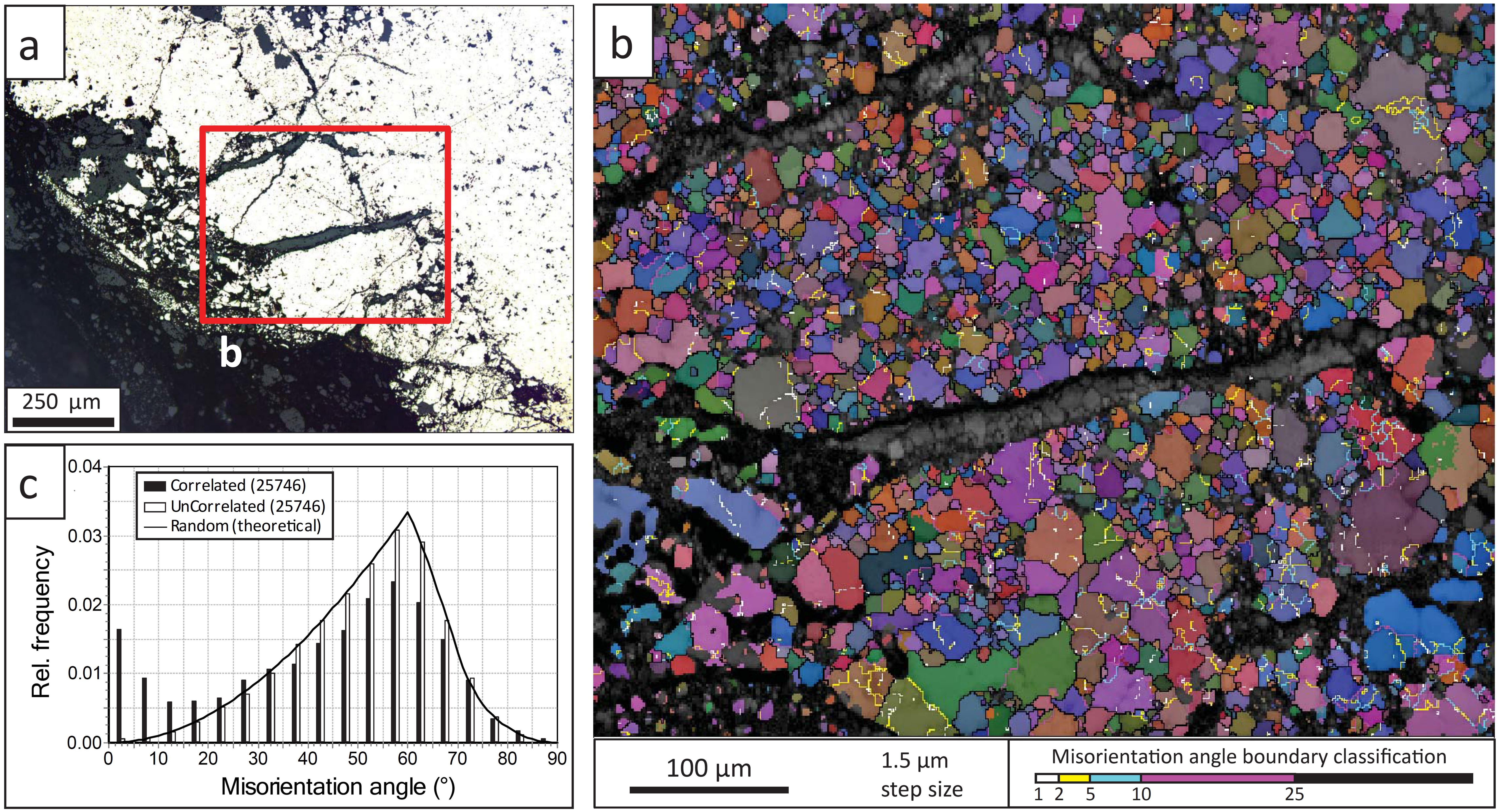

a
b
250 µm
c
Correlated (25746)
UnCorrelated (25746)
Random (theoretical)
Rel. frequency
0.04
0.03
0.02
0.01
0.00
0
10
20
30
40
50
60
70
80
90
Misorientation angle (°)
100 µm
1.5 µm
step size
Misorientation angle boundary classification
1
2
5
10
25

Fig. 11

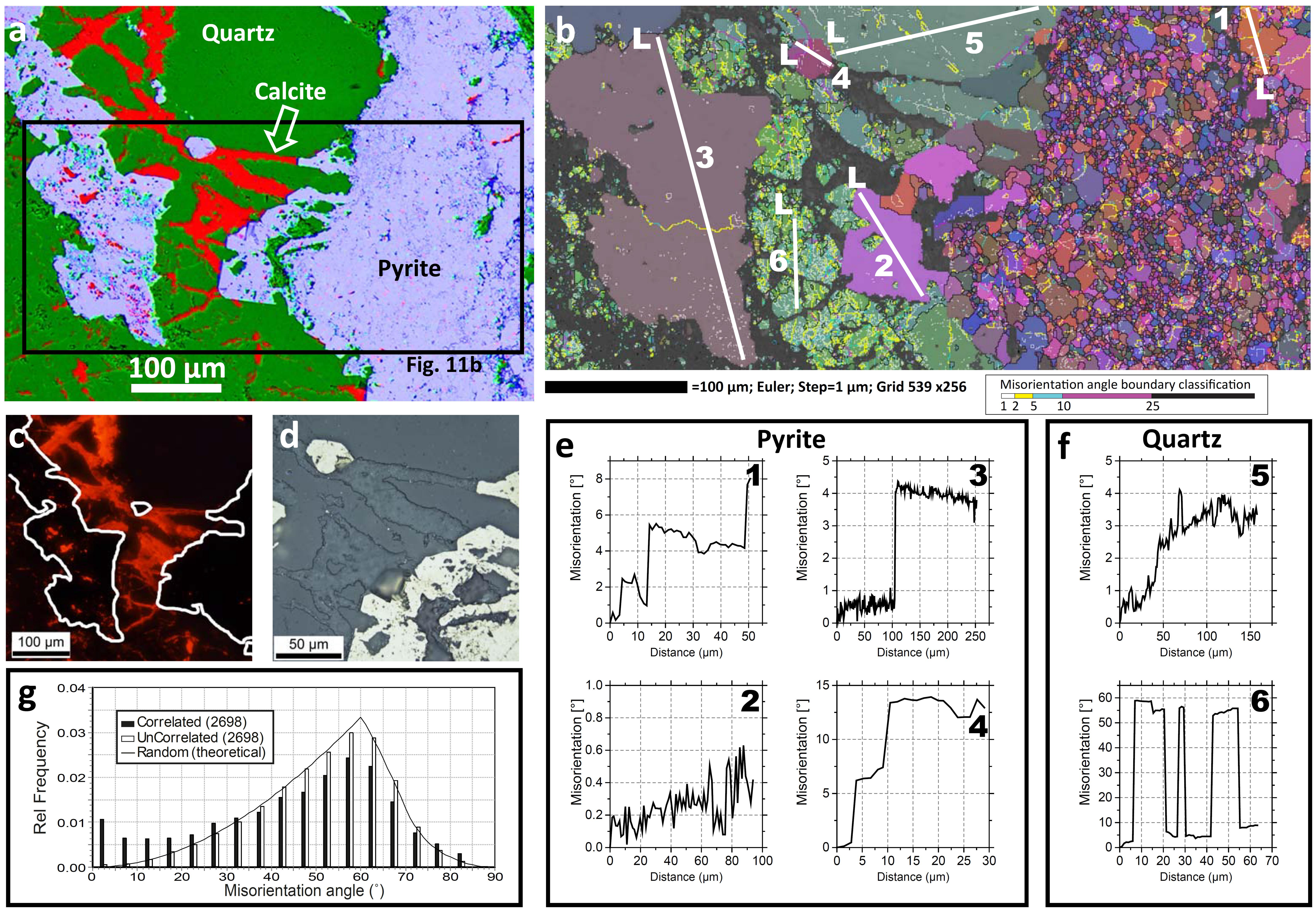

a
Quartz
Calcite
Pyrite
100 µm
Fig. 11b
b
=100 µm; Euler; Step=1 µm; Grid 539 x256
Misorientation angle boundary classification
1 2 5 10 25
c
100 µm
d
50 µm
e
Pyrite
Misorientation [°]
Distance (µm)
f
Quartz
g
Correlated (2698)
UnCorrelated (2698)
Random (theoretical)
Rel Frequency
Misorientation angle (°)

Fig. 12

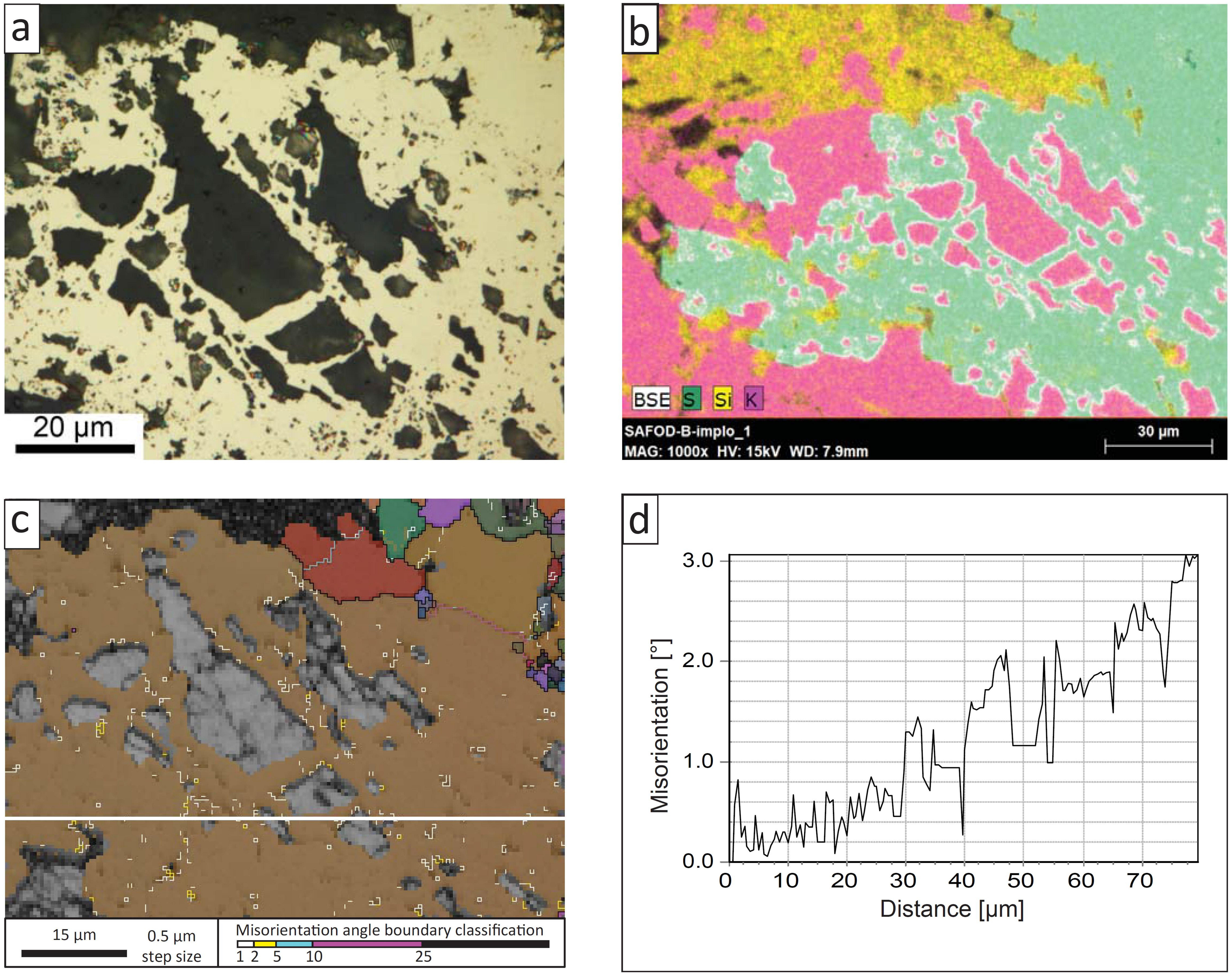
a
20 µm
b
BSE S Si K
SAFOD-B-implo_1
MAG: 1000x HV: 15kV WD: 7.9mm
30 µm
c
15 µm
0.5 µm step size
Misorientation angle boundary classification
1 2 5 10 25
d
Misorientation [°]
Distance [µm]
0.0
1.0
2.0
3.0
0
10
20
30
40
50
60
70

Fig. 13

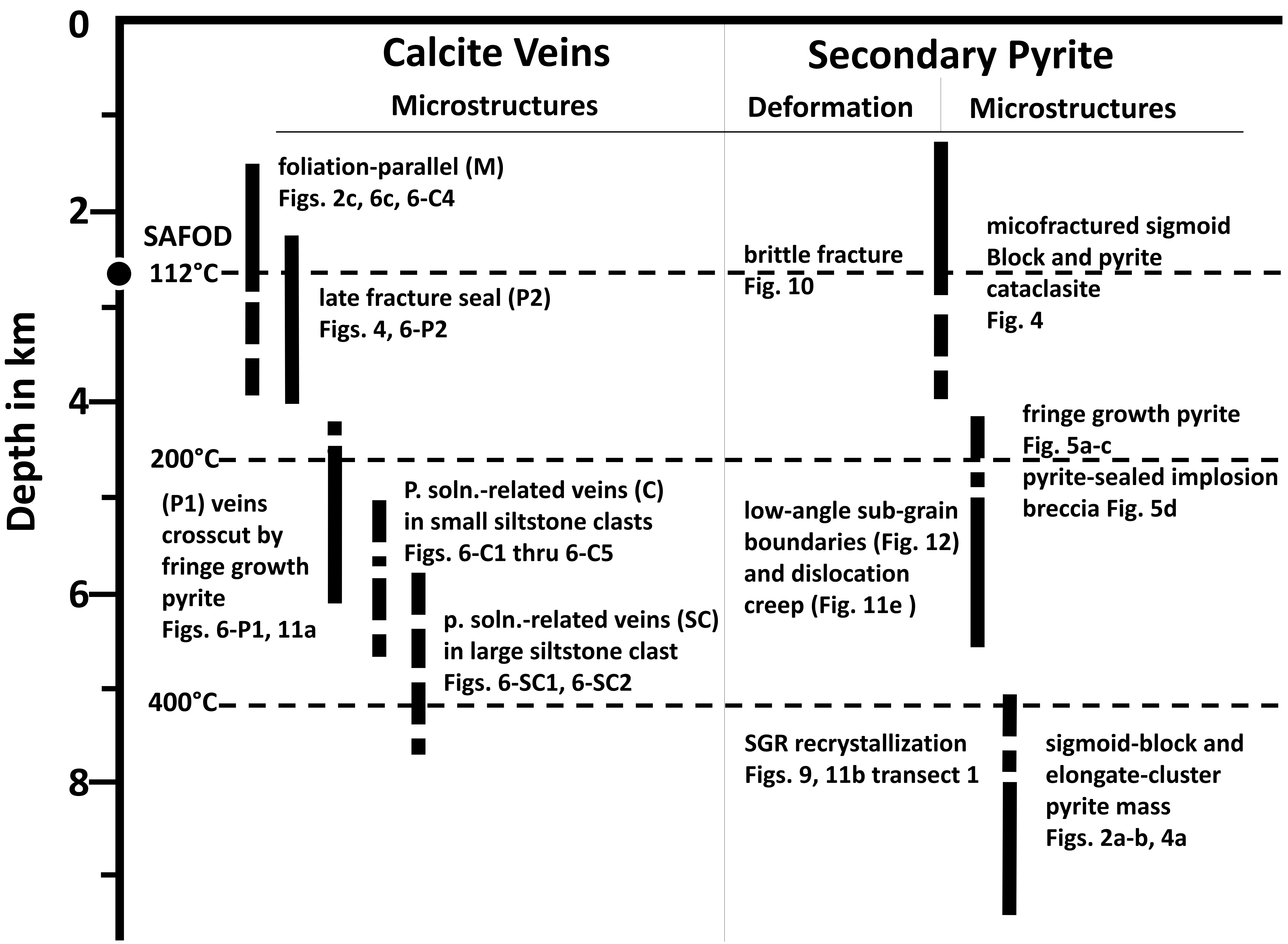

Depth in km
0
2
4
6
8
Calcite Veins
Microstructures
Secondary Pyrite
Deformation
Microstructures
SAFOD
112°C
200°C
400°C
foliation-parallel (M)
Figs. 2c, 6c, 6-C4
late fracture seal (P2)
Figs. 4, 6-P2
(P1) veins
crosscut by
fringe growth
pyrite
Figs. 6-P1, 11a
P. soln.-related veins (C)
in small siltstone clasts
Figs. 6-C1 thru 6-C5
p. soln.-related veins (SC)
in large siltstone clast
Figs. 6-SC1, 6-SC2
brittle fracture
Fig. 10
low-angle sub-grain
boundaries (Fig. 12)
and dislocation
creep (Fig. 11e)
SGR recrystallization
Figs. 9, 11b transect 1
micofractured sigmoid
Block and pyrite
cataclasite
Fig. 4
fringe growth pyrite
Fig. 5a-c
pyrite-sealed implosion
breccia Fig. 5d
sigmoid-block and
elongate-cluster
pyrite mass
Figs. 2a-b, 4a